



## Design, operation and analysis of wind-assisted cargo ships

Downloaded from: <https://research.chalmers.se>, 2024-04-26 16:42 UTC

Citation for the original published paper (version of record):

Tillig, F., Ringsberg, J. (2020). Design, operation and analysis of wind-assisted cargo ships. *Ocean Engineering*, 211(1): 1-23. <http://dx.doi.org/10.1016/j.oceaneng.2020.107603>

N.B. When citing this work, cite the original published paper.



# Design, operation and analysis of wind-assisted cargo ships

Fabian Tillig<sup>\*</sup>, Jonas W. Ringsberg

Chalmers University of Technology, Department of Mechanics and Maritime Sciences, Division of Marine Technology, SE-412 96, Gothenburg, Sweden

## ARTICLE INFO

### Keywords:

Energy systems model  
Flettner rotor  
Performance prediction  
Ship design  
Wind-assisted propulsion

## ABSTRACT

This study presents a novel approach to analytically capture aero- and hydrodynamic interaction effects on wind-assisted ships. Low aspect ratio wing theory is applied and modified to be used for the prediction of lift and drag forces of hulls sailing at drift angles. Aerodynamic interaction effects are captured by analytically solving the Navier-Stokes equation for incompressible, potential flow. The developed methods are implemented to a 4 degrees-of-freedom performance prediction model called “ShipCLEAN”, including a newly developed method for rpm control of Flettner rotors on a ship to maximize fuel savings. The accuracy of the model is proven by model- and full-scale verification. To present the variability of the model, two case study ships, a tanker and a RoRo, are equipped with a total of 11 different arrangements of Flettner rotors. The fuel savings and payback times are assessed using realistic weather from ships traveling on a Pacific Ocean route (tanker) and Baltic Sea route (RoRo). The results verify the importance of using a 4 degrees-of-freedom ship performance model, aero- and hydrodynamic interaction and the importance of controlling the rpm of each rotor individually. Fuel savings of 30% are achieved for the tanker, and 14% are achieved for the RoRo.

## 1. Introduction

To limit the consequences of climate change, society must dramatically reduce CO<sub>2</sub> emissions, which are a major driver of climate change (Anderson and Bows, 2011). With its large share of worldwide transport, shipping accounts for approximately 3% of global CO<sub>2</sub> emissions. The IMO set a goal to halve the emissions of the world's fleet by 2050 compared to the 2008 level (O and 2018. [Online]. Avai, 2018). At the same time, forecasts show a doubling of the transport needs by 2050, which has caused the world's shipping fleet to grow. Cutting the emissions of a growing fleet requires drastic measures and savings for each ship far exceeding the 50% decrease targeted for the entire fleet. Such a decrease in emissions cannot be achieved with conventional fuels, combustion engines and ship designs.

Alternative and complementary propulsion systems have become a focus of research in recent years. One such alternative is wind-assisted propulsion using, e.g., Flettner rotors, as shown for a tanker in Fig. 1. Although the implementation of wind-assisted propulsion in shipping is not without challenges, the large potential savings make it a viable solution concerning the environment and the economy (Rehmatulla et al., 2017).

Numerous studies have focused on the economics and general fuel savings of such systems (Ballnii et al., 2017; Talluri et al., 2018; Tillig

and Ringsberg, 2018; van der Kolk et al., 2019a), showing that wind-assisted propulsion can significantly lower fuel consumption and emissions. However, these studies have also shown that the economics highly depend on wind conditions, ship types and shipping routes.

Although several different wind propulsion technologies have been assessed, the most realistic options seem to be fixed-wing sails (or variants/combinations of wing sails) with or without flaps, rotor sails and kites (Traut et al., 2014; Lu and Ringsberg, 2019). In (Traut et al., 2014), the propulsive power contribution of a single Flettner rotor is compared with the power contribution from a kite, showing that the average savings with the single Flettner rotor are higher than with the kite. In (Viola et al., 2015), wing sails with flaps and twist control were applied to a tanker, and the results showed considerable power contributions that could save fuel.

The general characteristics of Flettner rotors have been widely studied by both CFD and model tests (Li et al., 2012; Bordogna et al., 2019). The potential savings of Flettner rotors applied to ships were shown in (Searcy, 2017) for domestic shipping, in (Tillig and Ringsberg, 2018) for a Baltic Sea route, in (Tillig et al., 2019) for an Atlantic triangular route and in (Bentin et al., 2016) for a trans-Atlantic route. All these studies show large potential savings and economic feasibility for Flettner rotors, while considering the installation and maintenance costs. Depending on the route, the ship type and the number of rotors, fuel savings approaching 40% have been reported. With such potential

<sup>\*</sup> Corresponding author.

E-mail address: [fabian.tillig@chalmers.se](mailto:fabian.tillig@chalmers.se) (F. Tillig).

**Nomenclature**

a	Factor for the induced drag [-]	$L_{oa}$	Length over all [m]
AP	Aft Perpendicular [-]	$L_{pp}$	Length between perpendicular [m]
AR	Aspect ratio [-]	$N_v$	Linear part of the yaw moment coefficient [-]
$A_R$	Rudder area [m <sup>2</sup> ]	$N_{vv}$	Nonlinear part of the yaw moment coefficient [-]
$AR_E$	Efficient aspect ratio [-]	P	Power [kW]
$A_{Rotor}$	Projected area of the rotor [m <sup>2</sup> ]	pdf	Probability density function [-]
AWA	Apparent wind angle [deg.]	r	Radius [m]
AWS	Apparent wind speed [m/s]	$R_c$	Radius of the vortex [m]
B	Beam [m]	$R_R$	Radius of the rotor [m]
b	Span of a wing [m]	SR	Spin ratio [-]
c	Chord length [m]	T	Thrust force [N]
$c_B$	Block coefficient [-]	$T_D$	Draft [m]
$c_D$	Drag coefficient [-]	TWA	True wind angle [deg.]
$c_{DI}$	Induced drag coefficient [-]	TWS	True wind speed [m/s]
CFD	Computational fluid dynamics [-]	u	Inflow speed [m/s]
$c_L$	Lift coefficient [-]	$u_A$	Wind speed (with boundary layer effect) [m/s]
$c_M$	Main frame area coefficient [-]	v	Speed [m/s]
$c_R$	Residual resistance coefficient [-]	$v_{des}$	Design speed [kn]
CoE	Center of effort [m]	$v_{hull}$	Forward speed of the hull [kn]
$c_P$	Power coefficient [-]	VMG	Velocity made good [kn]
$c_S$	Side force coefficient [-]	VPP	Velocity prediction program [-]
$c_T$	Thrust coefficient [-]	$v_S$	Ship speed [kn]
$c_{TH}$	Propeller thrust coefficient [-]	$v_{Service}$	Service speed [kn]
D	Drag force [N]	$v_T$	Tangential speed [m/s]
DOF	Degrees of freedom [-]	$\alpha$	Hellman exponent [-]
F	Force [N]	$\beta$	Drift angle [deg.]
FP	Forward perpendicular [-]	$\Gamma$	Circulation [m <sup>2</sup> /s]
$GM_0$	Metacentric height [m]	$\gamma$	Position of the external vortex [deg.]
h	Height [m]	$\gamma_R$	Flow straightening coefficient [-]
$H_S$	Significant wave height [m]	$\Delta$	Displacement [t]
$Y_v$	Linear part of the hull side force coefficient [-]	$\delta$	Rudder angle [deg.]
$Y_{vv}$	Nonlinear part of the hull side force coefficient [-]	$\nu$	Added speed at the suction side of a wing [m/s]
k	Ratio between $AR_E$ and AR [-]	$\rho_{Air}$	Air density [kg/m <sup>3</sup> ]
$k'$	Cross flow drag coefficient [-]	$\rho_{Water}$	Water density [kg/m <sup>3</sup> ]
L	Lift force [N]	$\Phi$	Heel angle [deg.]
		$\omega$	Angular speed [1/s]

savings and the ease of operation, Flettner rotors are one of the most promising propulsion alternatives for lowering shipping emissions.

Unlike the thrust from a propeller, the total force of a sail does not act along a ship's longitudinal axis. All sails produce a lift force perpendicular to the inflow and a drag force parallel to the inflow. These lift and drag forces can be transformed into a thrust in the ship's longitudinal direction and a side force perpendicular to the ship. The side forces

are much larger than the wind loads that are typically experienced by ships and must be compensated by a drift angle of the hull and a rudder angle, both of which create added resistance. To accurately predict the savings from wind-assisted propulsion, it is thus crucial to perform a four degrees-of-freedom (4 DOF) analysis of the ship, i.e. predict the yaw and heel moments, thrust and drift of the ship. For the performance prediction of the ship it is crucial to predict the added resistance from the

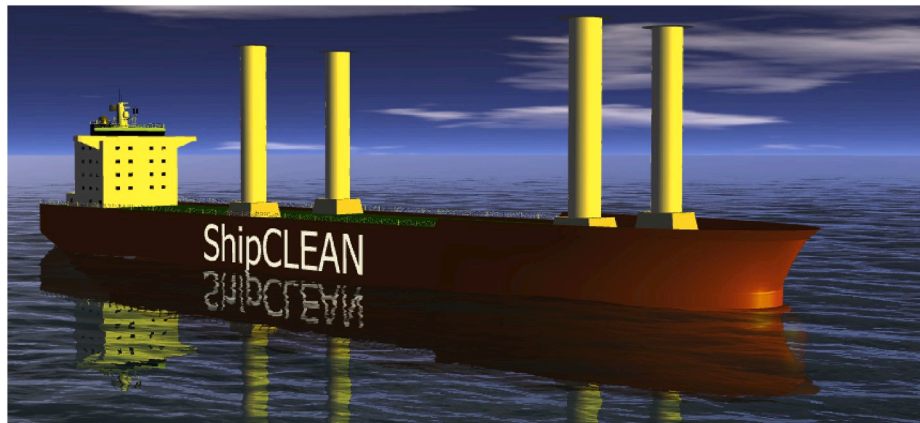


Fig. 1. Artist impression of a 180 m long tanker with 4 Flettner rotors (5 m × 30 m).

rudder which must compensate the yaw moment induced by the sails and the added resistance due to drift which appear due to the large side forces from the sails. Additionally, it is important to include the roll of the ship since, especially slender ships, can experience large heel angles due to the sails. A heel angle also introduces yaw moments from the sails due to the transversal shift of the thrust force and reduces the sail forces due to the reduced projected sail area. The importance of a systems perspective, including interaction effects in between the sails and between the sails and the hull, i.e., rudder angle and drift, is discussed in (Viola et al., 2015; van der Kolk et al., 2019b). In yacht sailing, models considering the sail and hydrodynamic forces that predict the performance of yachts are called velocity prediction programs (VPPs), and they are widely used to compare and predict the performance of sailing yachts. In shipping, such VPPs are not yet common. An approach towards a VPP was presented in (Tillig and Ringsberg, 2018; van der Kolk et al., 2019a; Viola et al., 2015). However, the main challenges remain quantifying the aerodynamic interaction and the hydrodynamics of ships sailing at a drift angle. In (Viola et al., 2015; Lee et al., 2016), the aerodynamic interaction effects were evaluated using time-consuming CFD computations, while the model in (van der Kolk et al., 2019a) was based on model tests. Typically, the hydrodynamics of a hull are based on empirical methods from maneuvering research, as in (Tillig and Ringsberg, 2018; Viola et al., 2015), or on CFD or model test results using standard series hulls (van der Kolk et al., 2019b; van der Kolk, 2016).

This study presents the continued development of a ship energy system model called ShipCLEAN, which was presented in (Tillig and Ringsberg, 2018). The new developments relate to modules in the ShipCLEAN model, which have been added to include the aerodynamic interaction effects and better represent the hydrodynamics of a ship sailing at a drift angle. Additionally, a novel approach to individually optimize the rpm of each Flettner rotor in an array installed on a ship is presented. The study focuses on the application of Flettner rotors because of their great potential for fuel savings and ease of operation; see the former references above.

To predict the feasibility and the potential savings of Flettner rotors on a large amount of different ships on different routes and to be able to perform optimizations of Flettner rotors on a ship, a simulation model must (i) be generic, i.e., require only a very limited amount of information about the ship, and (ii) require low computational efforts. With these requirements, the employed methods must rely on empirical or analytical formulations that together form a methodology and simulation model with known and acceptable prediction accuracy. CFD computations cannot be used for this purpose due to their computational effort, and model tests, especially for the rotors, cannot cover all possible arrangements and conditions for Flettner rotors on a ship. However, the ShipCLEAN model satisfies the above requirements—it is a simulation model specifically developed to provide accurate performance predictions with very limited input data with short computational time, thus being applicable to extensive studies as described above.

The article is divided into three main parts. In Section 2, the ShipCLEAN model is described. The theory of aerodynamic interaction and hydrodynamic lift and drag, as well as the implementation in ShipCLEAN, are discussed in Section 3. Section 4 discusses the operation, retrofitting and new design of wind-assisted propelled ships using examples with a tanker on a Pacific Ocean route and a RoRo on a Baltic Sea route, including the presentation of the rpm control of the rotors. A qualitative discussion of uncertainties of the predictions of the fuel savings is presented in Section 4.5, followed by the conclusions of the study in Section 5.

## 2. The ShipCLEAN model

The ShipCLEAN model is a ship performance prediction model based on analytical and empirical methods as well as on propeller and hull standard series, programmed in Matlab (Mathworks, 2020). The model

is developed following a modularized approach, i.e. each part of the model is represented by a module which can easily be replaced, or new modules can be added. All parts of the model are described in detail in (Tillig and Ringsberg, 2018) and (Tillig et al., 2017). In (Tillig et al., 2018), uncertainties in the prediction are analyzed and quantified. An overview of the model is shown in Fig. 2. The focus of the model development was that predictions should be available without numerous input data, e.g. the hull form and exact geometry of the ship shall not be necessary for a performance prediction. Thus, the data needed for a power prediction are the main dimensions ( $L_{oa}$ ,  $B$ ,  $T$ ,  $\Delta$ ), the design speed, the ship type and the propeller rpm. The remaining dimensions, such as the  $L_{pp}$ , depth, and superstructure dimensions, are estimated by the model using empirical formulas. The  $L_{pp}$  is estimated based on empirical bulb lengths and lengths of the ship aft of AP. The height of the superstructure is based on estimations of the number decks, and the length is depending on the size and type of the ship. As an example, PCTC and ferries are assumed to have superstructure lengths equal to their  $L_{pp}$ , tankers are assumed to have a superstructure length of 1/7th of their  $L_{pp}$ . Details about the estimation of the ship dimensions are presented in (Tillig, 2017). To predict the performance in real operation conditions, the true wind speed and angle (TWA, TWS), currents and water temperature must be specified. Wave heights and directions can be specified or evaluated to match the wind speed, a specified fetch and the wind direction. In (Tillig and Ringsberg, 2018), the ShipCLEAN model was extended compared to (Tillig et al., 2017, 2018) to handle 4 degrees of freedom (4 DOF), which was proven to be crucial for accurately predicting the performance of wind-assisted propelled ships. A detailed description of forces and moments acting on a wind-assisted propelled ship was presented in (Tillig and Ringsberg, 2018).

The focus when analyzing wind-assisted propulsion is on accurately predicting the delivered thrust of the sails and the hydrodynamic compensation of the side forces created by the sails. The forces and moments on a wind-assisted ship can be divided into two groups: (i) aerodynamic forces and moments, i.e., wind loads on the hull and superstructure as well as the sail forces and the resulting moments, and (ii) hydrodynamic forces and moments, i.e., drag and lift forces on the hull as well as rudder drag and lift forces and the resulting moments. The resistance of the hull is divided into calm water resistance, added resistance due to shallow water, added resistance due to waves, added resistance from fouling, added resistance from ice and added resistance due to drift. Additionally, the course and speed over ground are corrected for influences from ocean currents. A complete description of the employed methods can be found in (Tillig and Ringsberg, 2018; Tillig et al., 2017, 2018).

Since only the steady-state condition is evaluated in ShipCLEAN, the sum of all forces and moments in each of the 4 DOFs must be zero; see (Tillig and Ringsberg, 2018) for a complete description of the 4 DOF method in ShipCLEAN:

$$\sum F_x = \sum F_y = \sum N = \sum K = 0 \quad (1)$$

In addition to the surge, drift and yaw must be respected due to the high side forces and potentially high yaw moments that wind-assisted propulsion introduces. The consideration of the roll of the ship is crucial since heel angles can become large for slender ships with large sail areas and thus sail forces must be limited. Additionally, the projected area of the sails is reduced due to the heel angle (reducing the sail forces) and the thrust force from the sails are shifted transversely which causes a yaw moment. Since the forces and moments in the different directions are dependent on each other (e.g. the rudder drag is dependent on the propeller thrust, the drift angle and the rudder side force), equation (1) can only be solved iteratively. For a given sail force (e.g. given rpms of the installed Flettner rotors), the rudder angle, drift angle, heel angle and propeller thrust are iterated to achieve the force and moment balance. The starting point of the iteration is found by solving

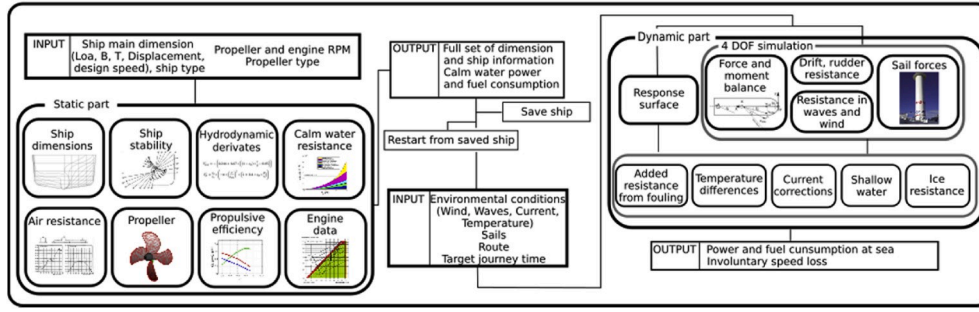


Fig. 2. Overview of the ShipCLEAN model.

equation (1) without the dependencies between forces and moments of different directions, i.e. the rudder forces are assumed independent of the propeller thrust and the resistance and sail forces independent of the heel and drift angles. Additionally, a novel rpm control iterates the rpm of each single rotor to minimize the required propeller thrust. The optimization is performed by stepwise reducing the rpm of selected rotors from the optimal rpm for the wind angle and speed. The selection of the rotor to reduce in power is performed using a scoring system, see Section 4.2.1 for details.

Since the ShipCLEAN model is based solely on empirical, analytical and interpolation methods, the computational time is significantly shorter than for models based on CFD. The evaluation of one weather condition for one target speed, including the hydro- and aerodynamic interaction (see Section 3), reefing (Section 4.2) and involuntary speed loss, takes approximately 10 s on a standard desktop PC. Without sails, this computational time reduces to less than 1 s.

The ShipCLEAN model was verified against a model test with different ship types in (Tillig et al., 2018) and full-scale measurements of a cruise ferry with a Flettner rotor installed in (Norsepower, 2019a). The results presented in (Tillig et al., 2018; Norsepower, 2019a) show very good agreement between the performance prediction using ShipCLEAN and the model- and full-scale measurements.

### 2.1. The Flettner rotor model in ShipCLEAN

The force generated by a Flettner rotor on board a ship is divided into a lift force (L), acting perpendicular to the local apparent wind direction and a drag force (D) acting in line with the local wind direction. With the local apparent wind direction, the lift and drag forces can be converted into thrust (T) and side (S) forces, as expressed in equations (2) and (3).

$$T = D \cos(AWA) - L \sin(AWA) \quad (2)$$

$$S = D \sin(AWA) + L \cos(AWA) \quad (3)$$

All forces are expressed using force coefficients as defined by equation (4).

$$c_i = \frac{i}{0.5 \rho A AWS^2}, \quad i = L, D, T, S \quad (4)$$

Since the Flettner rotors are rotated using electric motors, the power consumption must be respected in the performance prediction. The power consumption is expressed using a power coefficient  $c_p$ , as defined by equation (5).

$$c_p = \frac{P_{rotor}}{0.5 \rho A AWS^3} \quad (5)$$

The lift and drag force coefficients of a Flettner rotor depend on the spin ratio, the aspect ratio of the rotor and the size of the disc at the top. The spin ratio is defined as the ratio between the local wind speed (u in equation (6)) and the rotor's tangential speed at the surface.

$$SR = \frac{v_T}{u} = \frac{\omega R_R}{u} \quad (6)$$

In ShipCLEAN, the lift and drag coefficients are valid for rotors with an aspect ratio of  $AR = 6$  and with a disc diameter twice the rotor's diameter. The coefficients are based on the results in (Li et al., 2012) but corrected to better match the full-scale measurements, see Section 3.4.

$$c_L = -0.0046 SR^5 + 0.1145 SR^4 - 0.9817 SR^3 + 3.1309 SR^2 - 0.1039 SR \quad (7)$$

$$c_D = -0.0017 SR^5 + 0.0464 SR^4 - 0.4424 SR^3 + 1.7243 SR^2 - 1.641 SR + 0.6375 \quad (8)$$

$$c_p = 0.0001 SR^5 - 0.0004 SR^4 + 0.0143 SR^3 - 0.0168 SR^2 + 0.0234 SR \quad (9)$$

As described in Section 3, the forces and power consumption are analyzed for several rotational speeds at different heights. The initial rotational speed for one rotor is defined as the condition with the maximal net power for the rotor itself ( $P_{netRotor}$ ). Considering the number of heights  $n$ , the net power can be calculated by:

$$P_{netRotor}(SR) = P_T(SR) - P_{rotor}(SR) = \sum_{i=1}^n c_T(h, SR) \frac{\rho_{air} A_{rotor}}{2n} AWS(h)^2 u - c_p(h, SR) \frac{\rho_{air} A_{rotor}}{2n} AWS^3 \quad (10)$$

Note that equation (10) does not account for the added resistance from the drift and rudder angles. Based on the hydrodynamic response, i.e., the drift angle, the resistance and the rudder angle, reefing might be applied in the form of a reduced spin ratio to one or several rotors. Reefing and general operation of the rotors are described in Section 4.

## 3. Aero- and hydrodynamic interaction effects

To improve the methods presented in (Tillig and Ringsberg, 2018) for wind-assisted propulsion, the following sections focus on the interaction effects between sails, the superstructure and the hull of wind-assisted ships. New, improved methods for the prediction of the sail thrust and side force as well as for the lift and drag generated by a ship sailing at a drift angle are developed and presented.

### 3.1. Coordinate systems

Two coordinate systems are introduced, one fixed to the ship hull ( $x'$ ,  $y'$ ,  $z'$ ) and one flow oriented, fixed to the course through water ( $X, Y, Z$ ). Note that the course and speed corrections for ocean currents are performed prior to the analysis presented in this work, i.e., TWA, TWS and  $u$  are corrected for the influence of the ocean current. The coordinate



systems with the definition of the drift and rudder angles are shown in Fig. 3. The TWA and the wave encounter angle are defined counter-clockwise off the bow, i.e., an angle of zero degrees represents head wind/waves.

The force and moment balance according to equation (1) is done in the flow oriented (main) coordinate system (X, Y, Z). Therefore, forces from the ship-fixed coordinate system must be transferred to the main system:

$$F_X = F_{x'} \cos\beta + F_{y'} \sin\beta \quad (11)$$

$$F_Y = F_{y'} \cos\beta - F_{x'} \sin\beta \quad (12)$$

$$F_Z = F_{z'} \quad (13)$$

### 3.2. Wind speed gradient

The wind speed gradient describes the horizontal distribution of the mean wind speed, i.e., the interaction of the wind and the earth's surface or a ship's deck. Friction between the moving air and the earth's surface causes the wind speed to be lower the closer it is towards the earth, causing a boundary layer with characteristic wind speed profiles. The boundary layer thickness and shape are mainly influenced by the turbulence in the air and the shape/roughness of the surface.

The wind speed gradient can be described by (Kaltschmitt et al., 2007):

$$TWS(h) = TWS_{10} \left( \frac{h}{h_{10}} \right)^\alpha \quad (14)$$

where  $TWS_{10}$  is the wind speed at a height of 10 m ( $h_{10}$ ) and  $\alpha$  is the Hellmann coefficient, which is dependent on the surface of the earth and the turbulence of the wind at the point of interest. This wind speed gradient causes a shear of the apparent wind angle over the height of a sail on board a ship. In this study, two conditions are of interest: (i) the wind above the ocean surface, which is low in turbulence and stable due to the long fetch, and (ii) the wind above the ship's deck, which, due to the short fetch, is unstable. According to (Garzon and Figueroa, 2017), the Hellmann coefficient for stable air above the open water surface and unstable air above human inhabited areas is 0.27, which is chosen here for both abovementioned conditions.

The apparent wind speed and angles above the ship's deck are estimated in two steps. First, the apparent wind angle and apparent wind speed at 10 m height above the sea surface are computed using the true wind speed gradient over the sea surface as well as the true wind angle, the ship's speed and drift angle. Second, the apparent wind speed profile above the ship's deck is estimated using equation (14) with the assumption that the wind speed at 10 m above the deck is equivalent to the wind speed at the corresponding height (i.e. deck height + 10 m) above the sea surface. Fig. 4 shows the apparent wind angles and speeds at different heights of a rotor sail. Both the wind angle and the wind

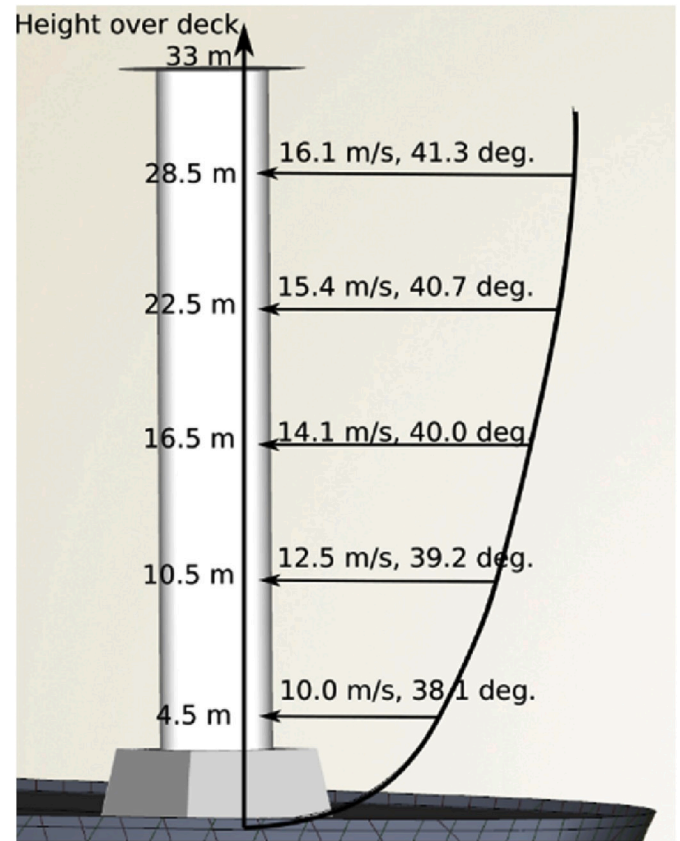


Fig. 4. Apparent wind speed and angle: sail height = 30 m, height of deck above the sea surface = 14 m,  $TWS_{10} = 7.3$  m/s,  $TWA = 60^\circ$ ,  $v_s = 10$  kn.

speed highly depend on the height above the deck. For a 30 m rotor sail, the speed is 60% higher at the top compared to the bottom, while the wind angle is  $3^\circ$  larger. These numbers show the importance of twist control of sails that require a certain angle of attack for specified wind speeds, such as wing sails. It must be noted that these angles are without the wind shear in the true wind that can be present and increase the differences.

Flettner rotors are not sensitive to the angle of attack. However, the rpm of the rotors must be optimized considering the wind speed and angle distributions since the thrust and side forces of the rotor depend on the local wind angle. For this reason, the forces, power consumption and moments of the sails are evaluated for several different rpms at each considered height. The maximum of the sum of the net power at each height (see equation (10)), i.e., the thrust power minus the consumed power, specifies the optimal rpm for the actual condition. The optimal rpms might be reduced later in the energy balance calculation in

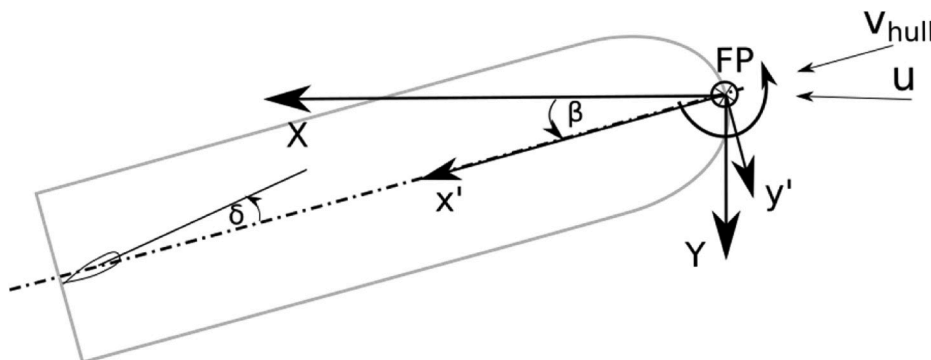


Fig. 3. Definition of coordinate systems.

ShipCLEAN due to the need to reduce the sail forces, as described in Section 4.1 and 4.2.

### 3.3. Sail-sail interaction

The influence of sails on the flow field across a ship's deck can be divided into two parts: (i) a potential part, i.e., a circulation that is induced into the flow field, and (ii) a viscous part, i.e., a wake and turbulence caused by flow separation and free vortices.

The induced circulation, i.e. the potential flow influence, results in a change in local wind speeds and directions across the ship and thus different wind conditions for each sail. A schematic presentation of the potential flow around a rotating cylinder is presented in Fig. 5, including the lift force  $L$ , drag force  $D$ , tangential speed  $v_T$ , rotational speed  $\omega$  and circulation  $\Gamma$ .

In (Garzon and Figueroa, 2017), the potential flow interaction effects are solved analytically for an array of Flettner rotors. Assuming a pure horizontal flow in the  $x$ - $y$  plane and defining the two boundary conditions as (i) the induced velocity at infinity is 0 and (ii) the induced speed at the rotor surface is equal to the tangential speed  $v_T$ , the Navier-Stokes equation can be simplified to an analytical solution of the flow pattern created by a single rotor (Garzon and Figueroa, 2017). The  $v_x$  (in the  $x$ -direction) and  $v_y$  (in the  $y$ -direction) components of the induced flows from the rotating cylinders can be computed by (Garzon and Figueroa, 2017) (with  $R_R$  as the radius of the rotor and  $v_T$  the induced velocity due to the circulation):

$$v_x(x, y) = \frac{v_T R_R}{\sqrt{x^2 + y^2}} \cos\left(\arctan\left(\frac{y}{x}\right)\right) \quad (15)$$

$$v_y(x, y) = \frac{v_T R_R}{\sqrt{x^2 + y^2}} \sin\left(\arctan\left(\frac{y}{x}\right)\right) \quad (16)$$

In equations (15) and (16), the rotor is assumed to be placed in the origin of the coordinate system. Since the solution is linear, the solution of an array of rotors is represented by the sum of the induced flow from each single rotor, given that the offsets from the coordinate center are considered for each rotor.

The induced velocity at the rotor radius can be computed using the circulation  $\Gamma$  which, according to the Biot-Sawert's law, can be expressed by (Houghton et al., 2017):

$$\Gamma = 2 \pi R_R v_T \quad (17)$$

The circulation  $\Gamma$  can be evaluated using known lift coefficients (e.g., from model tests) and the Kutta-Joukowski theorem (Abbot and Von Doenhoff, 1959) for the lift per unit span ( $L'$ , with  $u$  as the inflow

velocity):

$$L' = \rho^* u^* \Gamma \quad (18)$$

$$L' = c_L \frac{\rho^*}{2} u^{*2} c \quad (19)$$

This method can be used for any type of sail. For sails such as Flettner rotors, a more accurate relation between the lift coefficient and the circulation is given in (Swanson, 1961) as:

$$c_L = \left(1 - \left(\frac{R_R}{R_c}\right)\right) \left(\frac{\Gamma}{R_R U}\right) + \frac{\sin(\gamma)}{2\pi} \left(\frac{R_R}{R_c}\right) \left(\frac{\Gamma}{R_R U}\right)^2 \quad (20)$$

Here, the term  $\left(\frac{R_R}{R_c}\right)$  stands for the relation between the radius of the rotor ( $R_R$ ) and the distance to the external vortex ( $R_c$ ), and  $\gamma$  describes the location of the external vortex (Swanson, 1961). Unfortunately,  $\left(\frac{R_R}{R_c}\right)$  and  $\gamma$  cannot be found analytically. In (Swanson, 1961), for spin ratios between 1 and 4, good agreement with the model test results was obtained with  $\left(\frac{R_R}{R_c}\right) = 0.25$  and  $\gamma = 210^\circ$ . In Fig. 6a, the angular speed of

a Flettner rotor with 5 m diameter and 30 m height is compared to the angular speed of the fluid, computed from the circulation according to equation (20). Additionally, in Fig. 6b, the angular speed computed from the circulation according to equation (20) is compared to the angular speed according to equation (18). The circulation reaches a maximum at a spin ratio of approximately 4. Fig. 6a shows that the angular speed computed from equation (20) is slightly higher than the speed computed from equation (18). Since equation (20) proposed in (Swanson, 1961) is specifically for Flettner rotors, it is used in this study. For other sail types, such as wing sails, the formulation in equations (18) and (19) can be used to predict the interactions according to equations (15) and (16).

Equations (15)–(20) can be solved analytically to calculate the flow field in an array of Flettner rotors. However, since the optimal rpm of a rotor depends on the local wind speed and angle and the induced velocities depend on the rotor's rpm, an iteration is required to achieve the flow field respecting the optimal rpm of each rotor. Note that, in this stage, the optimal rpm is calculated without respecting the drift and rudder forces, which are first included in the rpm optimization, see Section 4.1.1. To visualize the interaction effects, a tanker with 4 Flettner rotors (5 m in diameter and 30 m high) is studied at a ship speed,  $v_s$ , of 12 kn and a TWS of 12 m/s. The rotors are arranged in a rectangular array with a longitudinal distance of 61.2 m and a transverse distance of 25.8 m (see Fig. 7). The induced flow field according to equations (15) and (16) is shown for a TWA of  $65^\circ$  (AWA =  $45^\circ$ , AWS = 16.5 m/s). Additionally, the wind angles and wind speeds experienced by each of the rotors are shown. Both the wind angle and the wind speed experienced by each rotor are highly influenced by the presence of the other rotors. Thus, the thrust and side force coefficients and optimal rpm must be evaluated respecting the local wind speed and angle. Naturally, the pattern of the wind angles and wind speeds for each rotor correspond to those experienced by sail boats on different positions in a fleet race (Bethwaite, 2013).

The viscous interactions are comprised of a wake, i.e. areas of low wind speed due to flow separation, and free vortices created by the rotors. In (Bordogna et al., 2020) it is shown from flow measurements in model tests, that the wake behind a cylinder diminishes as it spins. This indicates that there should not be any wakes behind Flettner rotors. However, in e.g. (Bethwaite, 2013) it is presented that sail boats further downwind in a fleet of racing sail boats experience lower wind speeds and high turbulence in the air. Since every sail creates tip vortices, depending on the generated lift, it is most likely that such vortices influence the air flow to the sails further downwind. In the horizontal plane, tip vortices are following the potential streamlines. However, the vertical path, i.e. the height of the vortices and the diameter are more

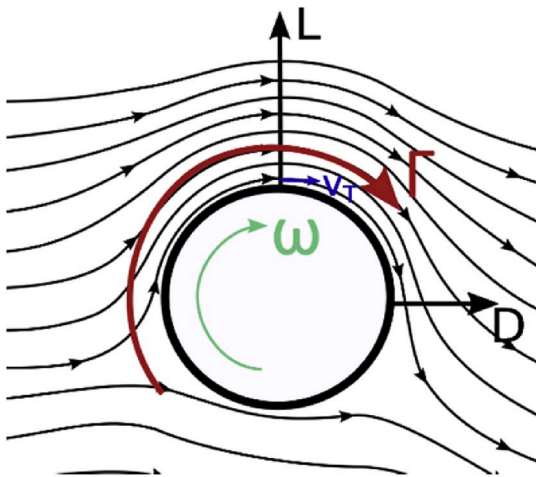


Fig. 5. A schematic of the potential flow around a rotating cylinder.

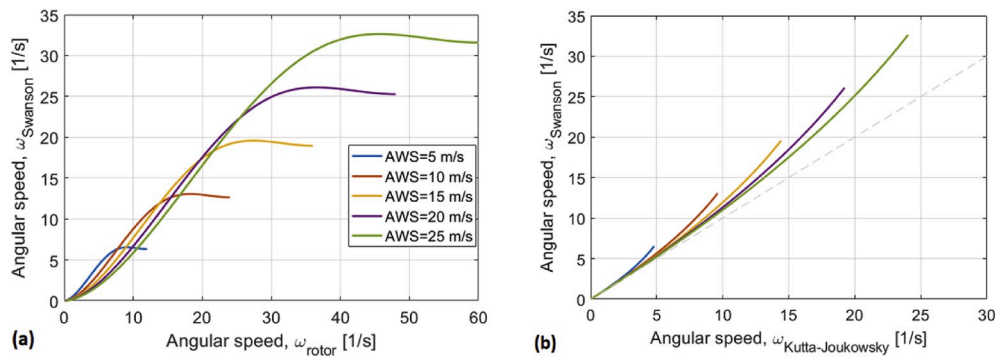


Fig. 6. Comparison of the angular speed of the rotor and the fluid and the angular speed of the fluid evaluated by (a) Swanson (Garzon and Figueroa, 2017) and (b) the Kutta-Joukowski theorem (Kaltschmitt et al., 2007).

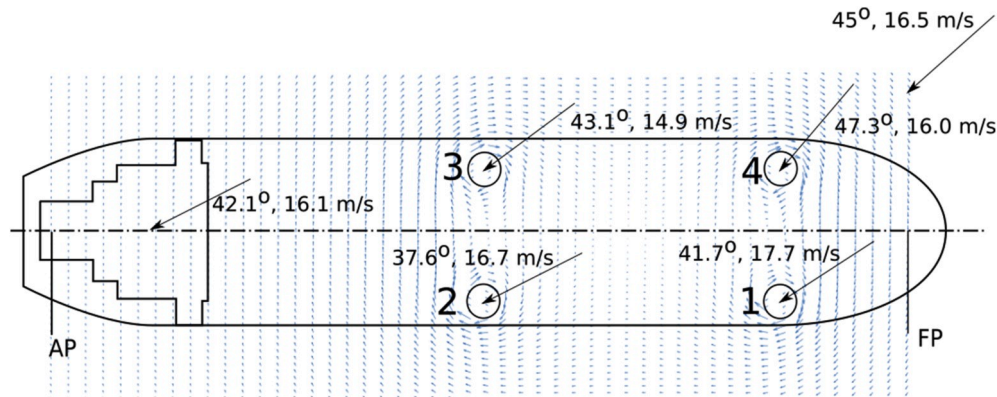


Fig. 7. Induced flow for an array of four Flettner rotors including the local wind angles (AWA) and speeds (AWS) for each rotor; TWA = 65°; TWS = 12 m/s;  $v_s$  = 12 kn.

difficult to predict without flow measurements or CFD computations. In ShipCLEAN, the focus is on fast predictions of the performance of wind-assisted ships without requiring detailed information to, e.g., enable easy weather routing. Thus, CFD computations cannot be used but eventual performance penalties due to turbulent air or free vortices must be captured. To reduce the performance of sails downwind of another sail, the wind speed is reduced in an area with a width of the chord length (or diameter for Flettner rotors) along the potential streamlines downwind of a sail. In ShipCLEAN, a standard wind speed reduction of 5% compared to the local wind speed including the potential influences is applied. A visualization of the sum of all flow

influences is presented in Fig. 8. Note that the flow reduction due to the viscous interactions in Fig. 8 is exaggerated and set to 15%, to better visualize the vortex paths. Additionally, the deck house and its influence on the flow is visible as a rectangle in the left side of Fig. 8. The interactions caused by the superstructure are further discussed in Section 3.4.

In Fig. 9, the thrust from the rotors arranged according to Fig. 7 is shown for TWA from 0 to 360°, including the potential (a) and viscous flow (b) interaction effects. For the latter case, the wind speed reduction is exaggerated and set to 15% to better visualize the impact. All rotors are operated at the maximum net-thrust point. It can clearly be seen that

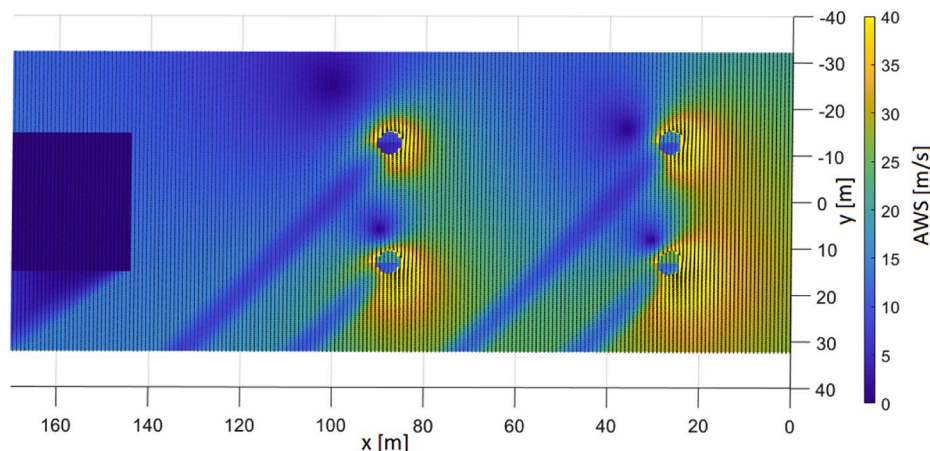
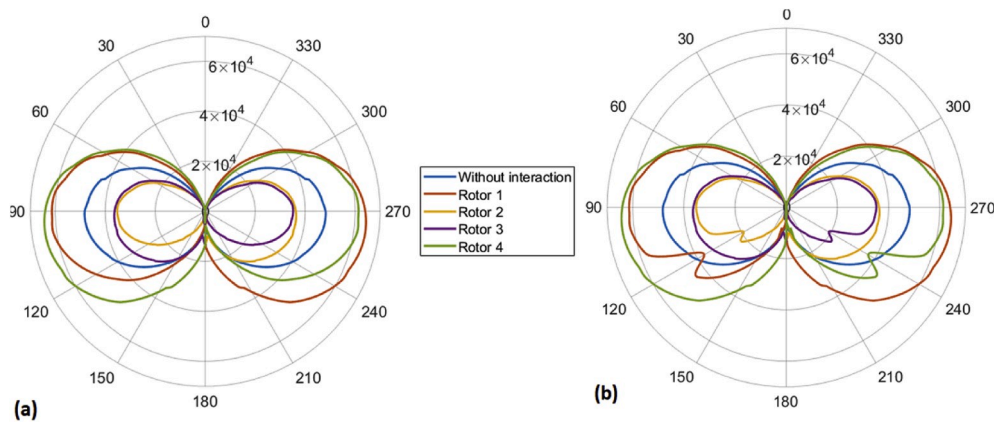


Fig. 8. Wind speeds at 10 m above deck including the superstructure (see Section 3.4); TWS = 12 m/s;  $v_s$  = 12 kn; TWA = 65°.





**Fig. 9.** Thrust force [N] vs true wind angle (TWA [deg.]) from rotors with and without interaction effects: (a) potential flow and (b) potential flow and viscous, TWS = 12 m/s,  $v_s = 12$  kn.

the forward rotors, i.e., numbers 1 and 4, largely benefit from the interaction with the other rotors, while rotors 2 and 3 suffer. The decrease in performance for rotors in a vortex path can be seen for rotor 1 at approximately  $120^\circ$  TWA (approximately  $90^\circ$  AWA) and for rotor 4 at approximately  $240^\circ$  TWA (approximately  $270^\circ$  AWA). Additionally, rotor 2 is in the path of rotor 4 at approximately  $20^\circ$  AWA, while rotor 3 is in the path of rotor 1 at approximately  $340^\circ$  AWA. Without the viscous interaction, the total thrust from all four rotors is slightly higher (less than 1%) if computed with potential interaction compared to the thrust without interaction. This increase can be explained by the circulation that is built up around the array of rotors, comparable to the circulation around the head and main sail of a yacht (Bethwaite, 2013). It must be noted that the side forces created by the sails are also increased due to the flow interactions. During the rpm optimization (see Section 4.2.1), rotor 1 is often “reefed” (reduced rpm) due to the high side forces it creates.

Comparing the results with and without flow interaction, the center of effort of the side force differs by 6–30%, with the center of effort evaluated with interaction effects being further forward. This difference has a large impact on the overall performance of the ship due to the interaction effects with the hull (see Section 3.5). Furthermore, reliable rpm control of the rotors (see Section 4.2.1) is only possible if the local wind speed and angle are estimated. Both the rpm control and the difference of the center of effort prove it crucial to include aerodynamic interaction effects when evaluating the performance of wind-assisted propulsion with more than one sail installed on the ship. It must be concluded that the dominating part of the aerodynamic interaction is potential part, i.e. the induced circulation, causing a change of the local wind speeds and angles. Furthermore, the results of the simulated aerodynamic interactions and the forces generated by the Flettner rotors are verified against model and full-scale measurements in Section 3.5.

### 3.4. Sail-superstructure interaction

The presence of working sails ahead or behind a superstructure changes the angle and velocity of the inflow. The local wind speed and angle at the position of the superstructure are calculated using the method described in Section 3.3. An example is presented in Fig. 7. Additionally, the superstructure can affect the sails if a sail occurs in the upstream vortex or in the downstream wake (Meroney, 1985). However, this will only occur in a small range of wind angles, such as close to stern wind, and close to head wind, both of which are not favorable conditions for sailing. The model described below is thus simplified and only intended to capture the decrease of forces of the idling rotors for the above conditions.

As shown in (Meroney, 1985), the upstream vortex only affects an area of the height of less than  $1/3$  of the superstructure height and

extends less than half of the height forward. Thus, the upstream vortex is neglected in this study. The downstream wake is modeled using a sinusoidal reduction of the wind speed, from zero at the superstructure until it reaches the free wind speed at a distance equal to 20 times the height of the superstructure; this agrees with the measured wake behind buildings in (Meroney, 1985). The wake behind the superstructure is visualized in Fig. 8.

### 3.5. Verification of the aerodynamic forces

The sail module of ShipCLEAN, i.e. the formulations to calculate the lift and drag as well as the method to evaluate aerodynamic interactions, have been compared to results from CFD, model tests and full-scale measurements. In a first step the lift, drag and power coefficients of a single Flettner rotor are compared between (i) full-scale measurements, (ii) ShipCLEAN simulations, (iii) CFD results from (Li et al., 2012; Kramer et al., 2016), and (iv) model test results from (Bordogna et al., 2020). The full-scale measurements were collected on-board a cruise ferry with a single  $4 \times 24$  m Flettner rotor installed (Norsepower, 2019a). The total thrust and side force were measured using force transducers at the foundation of the rotors. The power needed to rotate the rotor was measured as the power consumption of the electric motor installed for the rotor. Wind speed and angle were measured with the ship’s own instruments. Measurements were only taken in static sailing conditions, i.e. constant ship speed and heading. Fig. 10 presents the results from the comparison. For the analysis, the wind speed profile as presented in Section 3.2 is applied to calculate the wind speed experienced by the Flettner rotor.

Since no data filtering was applied, the results from the full-scale measurements show some scatter. However, clear clusters of measurement results can be found for both, the lift and drag coefficients and the power coefficients. The comparison in Fig. 10a shows that the lift coefficient in the full-scale measurement is considerably higher than the lift coefficient predicted in (Li et al., 2012) and measured in model scale in (Bordogna et al., 2020). At a spin ratio of  $SR = 3$ , for example, the results from (Bordogna et al., 2020) show a lift coefficient of about 6.5, the results from (Li et al., 2012) about 8.5 and the ShipCLEAN simulations of the full-scale measurements give a lift coefficient of about 9.5. It must be noted that the aspect ratio of the rotors in (Bordogna et al., 2020) is  $AR = 5$  compared to  $AR = 6$  in the full-scale measurements and in (Li et al., 2012; Kramer et al., 2016). In the study presented in (Bordogna et al., 2020), tests at different Reynolds numbers ( $Re$ ) were performed. The results indicate a considerable scale effect with the lift forces increasing with increasing Reynolds number. This could explain the higher measured lift forces in full scale. Fig. 10b shows that the results of the drag coefficient align well for spin ratios larger than 1. At  $SR$  lower than one the ShipCLEAN simulations give lower values. At a spin

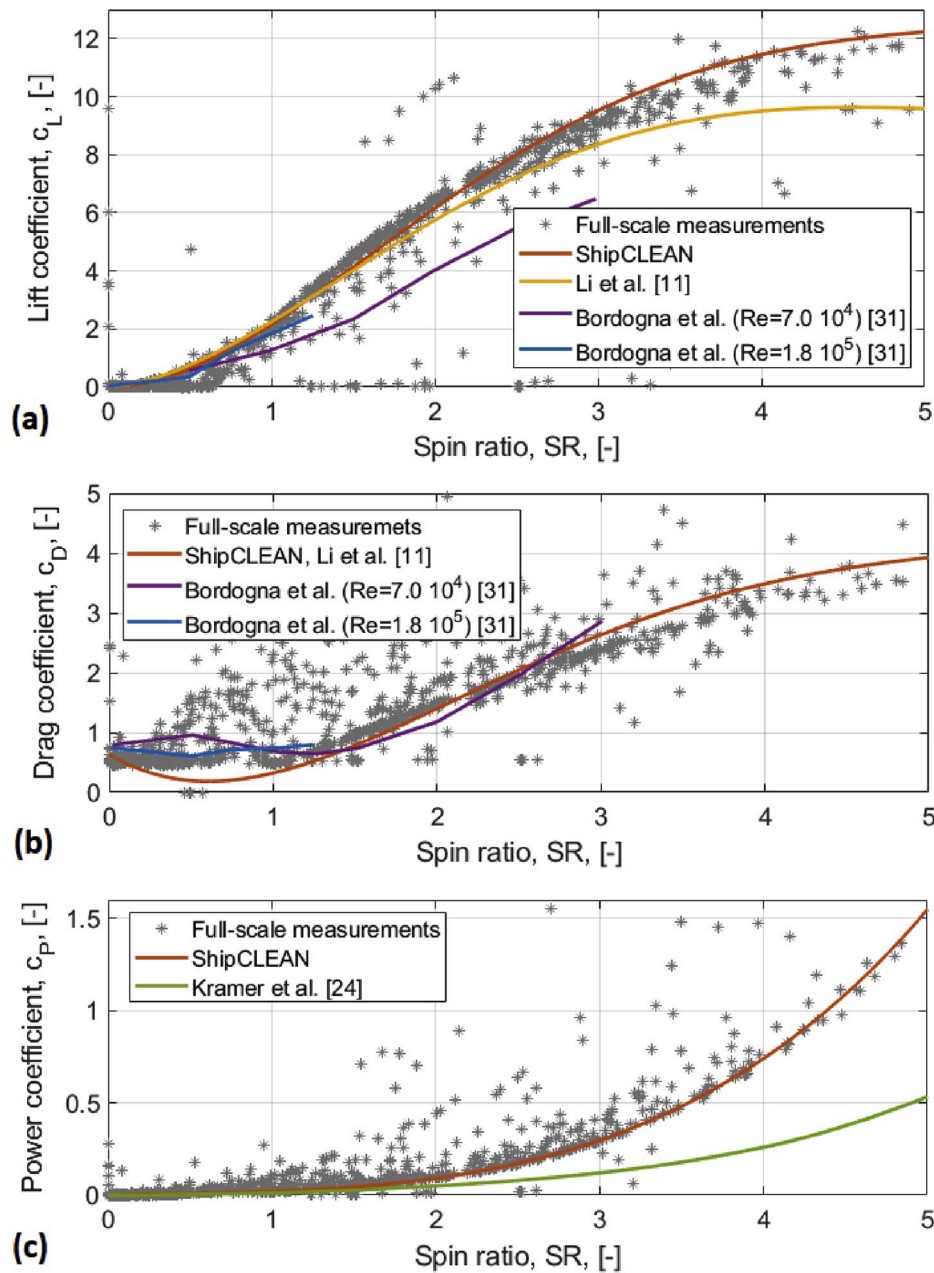


**Fig. 10.** Comparison of force and power coefficients between full scale measurements, ShipCLEAN simulations, CFD results from (Li et al., 2012; Kramer et al., 2016) and model test results from (Bordogna et al., 2020): (a) lift coefficient, (b) drag coefficient, and (c) power coefficient.

ratio of  $SR = 0.5$ , the ShipCLEAN simulation gives a value of about 0.3, while the full and model scale measurements show values of about 0.5–0.8. This underprediction will reduce the penalties of installed Flettner rotors in head wind. Fig. 10c shows that the power coefficient in (Kramer et al., 2016) underestimates the actual measured power in full scale. This is expected since the results in (Kramer et al., 2016) do not include any losses due to friction in the bearings or losses in the electrical motor. It must be noted, that the lift, drag and power coefficients generally show worse agreement at high spin ratios. However, in typical operation a spin ratio of around 1.5–2.5 is often optimal. In this range the different methods and results agree better.

In a second step, the sail interaction was verified by comparing the performance of two Flettner rotors placed along the longitudinal axis with a distance of 3 rotor diameters. The forward rotor was denoted as rotor A. The tested conditions are summarized in Table 1. Results of the ShipCLEAN simulation and from the model tests in (Bordogna et al.,

**Table 1**

Test case definition for the verification of aerodynamic interaction.

Case ID	Rotor distance	SR, rotor A	SR, rotor B
(a)	3 x $D_{rotor}$	2	2
(b)	3 x $D_{rotor}$	1	1.5

2020) are presented in Fig. 11a for case (a) and Fig. 11b for case (b).

From Fig. 11 it can be concluded that the thrust coefficients from measurements and ShipCLEAN predictions show similar trends. In beating conditions, the thrust coefficient is significantly reduced, up to 38% according to measurements at  $30^\circ$  AWA in case (a). In reaching conditions the thrust coefficient is increased with up to 7% for case (b). The side force coefficients are increased in most conditions due to the interaction effects. For case (a), the ShipCLEAN predictions are lower than the model test results for beating conditions but do not include the

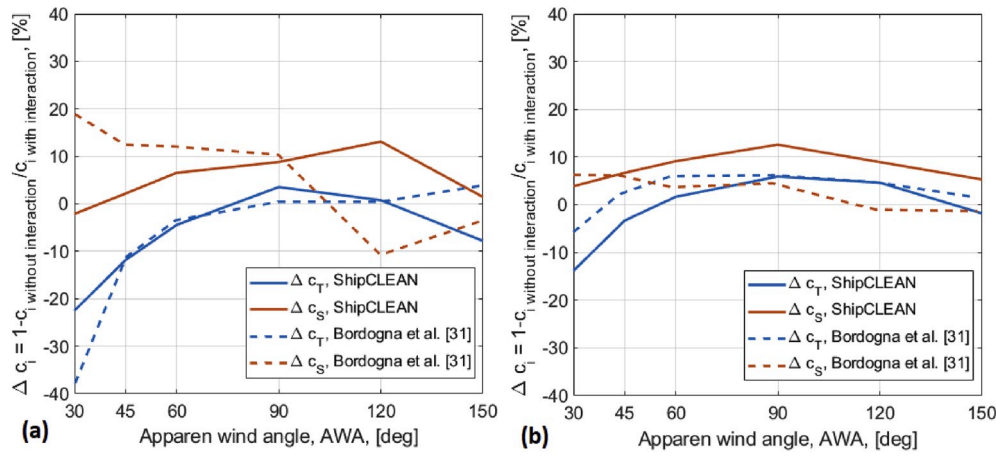


**Fig. 11.** Predicted and measured difference of the thrust and side force coefficients of two Flettner rotors with and without aerodynamic interaction, a) SR = 2 for both rotors, b) SR = 1 for rotor A and SR = 1.5 for rotor B.

sudden decrease of side force shown in the measurement results at around 120° AWA. As discussed in (Bordogna et al., 2020), model test results also include significant uncertainties, which might cause this sudden decrease. Alternatively, some effects are not captured by the method in ShipCLEAN. For case (b) ShipCLEAN overpredicts the influences on the side force when compared to the model tests results. For case (b) and an AWA of 90°, ShipCLEAN shows an increase of the side force with 11%, compared to the 5% in the measurement results. It must be kept in mind that the Flettner rotors in ShipCLEAN and in the model tests have different aspect ratios and different lift and drag coefficients, see Fig. 10. Since the potential flow interactions are coupled to the induced circulation, which is coupled to the lift generation of the Flettner rotors, this difference will influence the absolute values in the comparison. From the results it must be concluded that the method presented in Section 3.3 shows good agreement with the trends for the thrust and side force when compared to model test results. The side force might be overpredicted, which leads to a somewhat conservative prediction of the total performance of a ship. It must further be noted that the presented results are for rotors at a fixed SR related to the free stream velocity. As discussed in Section 3.3, the differences in total performance can be much smaller than the difference shown here, since the rotors can be operated at an optimal spin ratio for the local wind speed and angle.

### 3.6. Sail-hull interaction

Since the sails introduce large side forces on the ship, the main concern in the hydrodynamic interaction between the sails and the hull is the compensation of the introduced side force by drifting and rudder forces. The distribution of the side force between the rudder and the hull is coupled to the superstructure and the position of the rotors, since the rudder must compensate for the yaw moment introduced by the windage and the sails. The lift and drag forces are computed by:

$$L = c_{L\frac{\rho}{2}} u^2 L_{pp} T \quad (21)$$

$$D = c_{D\frac{\rho}{2}} u^2 L_{pp} T \quad (22)$$

The rudder forces can be computed using basic wing theory, which in ShipCLEAN is implemented by the formulas given in (Bertram, 2000):

$$\dot{x}_R = c_{Dv_s^2} \frac{\rho}{2} A_R + T \left( 1 + \frac{1}{\sqrt{1 + c_{Th}}} \right) (1 - \cos \delta_R) \quad (23)$$

$$y'_R = c_{Lv_s^2} \frac{\rho}{2} A_R + T \left( 1 + \frac{1}{\sqrt{1 + c_{Th}}} \right) \sin \delta_R \quad (24)$$

$$c_L = 2\pi \frac{AR^*(AR + 0.7)}{(AR + 1.7)^2} \sin \delta_R + \sin \delta_R |\sin \delta_R| \cos \delta_R \quad (25)$$

$$c_D = \frac{c_L^2}{\pi^* AR} + |\sin \delta_R|^3 \quad (26)$$

The rudder angle  $\delta_R$  is the corrected angle to account for the drift of the ship and the flow straightening from the aft body (Kijima et al., 1990):

$$\delta_R = \delta - \gamma_R \beta \quad (27)$$

$$\gamma_R = -22.2 \left( \frac{B}{L_{PP}} \right)^2 + 0.02 \left( c_{B\frac{B}{L_{PP}}} \right) + 0.68 \quad (28)$$

To verify and adjust a method to evaluate the lift and drag of a ship hull at drift, three sets of model test results are used in this study: (i) model tests of a Series 60 hull reported in (Longo and Stern, 2002), (ii) model tests and CFD computations of a series of hulls with different block coefficients (hull 1  $c_B = 0.72$ , hull 16  $c_B = 0.83$  and hull 19  $c_B = 0.64$ ) reported in (van der Kolk et al., 2019b), and (iii) model tests of a tanker reported in (Kume et al., 2006). It must be noted that the side force, moment and the induced resistance at small drift angles are small values compared to the ship's resistance. Thus, large deviations can be expected, as discussed and shown in (Kume et al., 2006). In (Kume et al., 2006), the standard deviations for the resistance, side force and moment were evaluated to be approximately 3.5%, keeping in mind that the measured resistance includes the resistance without drift, which will increase the uncertainty of the induced resistance. In (van der Kolk et al., 2019b), it has been shown that the difference between simulation results and model test results is the largest for the induced drag. It should also be noted that side forces and added resistances are often given in the ship fixed coordinate system and must thus be converted to the lift and drag forces in the flow-oriented coordinate system, which is used in this study.

The side force and drag due to drift are often estimated using empirical methods for maneuvering, e.g., according to (Inoue and Hirano, 1987). However, as shown in Fig. 12, the side force is highly overpredicted (up to 400%) when using this method compared to the data presented in (van der Kolk et al., 2019b; Kijima et al., 1990; Longo and Stern, 2002). Thus, the method proposed in (Inoue and Hirano, 1987) is found unsuitable for the analysis of the static sailing condition of wind-assisted propelled ships. Fig. 12 also shows that hull 16 of the Delft series has significantly higher lift forces than the other two hulls in the series, even though the only difference is the block coefficient.

To analyze the hydrodynamic response of wind-assisted propelled ships, three parameters are crucial: (i) the hydrodynamic lift, (ii) the

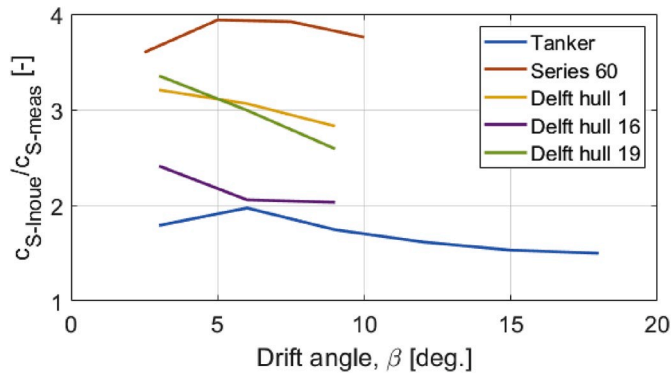


Fig. 12. Comparison of the measured (meas) side force coefficient with the predicted (Inoue) coefficient according to (Inoue and Hirano, 1987).

hydrodynamic drag, and (iii) the center of effort of the lift force. As explained in Sections 1 and 2, the ShipCLEAN model is intended to provide fast predictions with a very limited input, i.e., only the main dimensions of a ship. Thus, more sophisticated methods for the prediction of the abovementioned force and moment parameters, such as the method in (Hooft, 1996) or CFD computations, cannot be applied since the hull form is unknown and the computations would be too time consuming. Alternative methods could be to (i) build up data bases of results with standard series hulls using model tests, (ii) CFD computations, or (iii) to apply theoretical methods using only the main parameters of the hull, which is done in this study. The following section describes in detail how the side force, drag and yaw moment are evaluated using wing theory for small aspect ratio wings. Low aspect ratio (AR) wings are defined as wings with  $AR < 4$  (Hoerner, 1985). Cargo ships have aspect ratios (draft to length ratios) of well below one and are thus suitable to be analyzed with the low aspect ratio wing theory. According to the theory for the lift and drag of low aspect ratio as presented in (Hoerner, 1985), the potential flow lift and induced drag are only influenced by the efficient aspect ratio of the wing. The relation between the aspect ratio and the efficient aspect ratio depends mainly on the rounding of the edges (i.e., the bilge radius) and the planform. Additionally, a cross flow drag is considerable for small aspect ratio wings. In summary, one goal of the study is to relate the lift and drag of a hull to its aspect ratio and possibly the block coefficient or main frame area coefficient.

### 3.6.1. Limitations of the model

The presented model implemented in ShipCLEAN can only be applied on drift angles where there is circulatory lift, i.e., below the angle of maximum lift. In (Hoerner, 1985), it was shown that this angle is expected to be 20–40° for aspect ratios close to those of ships, which is much higher than reasonable drift angles for static ship operations.

In (van der Kolk, 2016; Inoue and Hirano, 1987), it was discussed that the wave pattern affects the lift and drag of a ship hull. However, the low aspect ratio wing theory does not account for two phase flows; thus, these effects will not be captured unless the coefficients can be related to the residual resistance  $c_R$ .

As discussed in (Houghton et al., 2017; Hooft, 1996), the form of the leading edge of a wing section (bow shape), the planform shape (lateral plan) and edges (bilge) have a significant influence on the lift and drag characteristics. Due to the limited and simplified input to the ShipCLEAN model, such hull form features are unknown (i.e., not required as input) and thus cannot be considered unless the effects can be related to form parameters such as the block, prismatic or main frame area coefficient. Due to the nature of ShipCLEAN, the ships are assumed to be of conventional shape, e.g., have a full lateral plan.

### 3.6.2. Hydrodynamic lift forces of the hull

To estimate the lift and drag of the hull at a drift angle in a more theoretical way, two approaches can be used: the lifting line/wing theory or the slender body theory. The slender body theory is often applied to cylinder shapes, e.g., in (Jorgensen, 1973) and (Barros et al., 2008). It was shown that the slender body theory well predicts the lift force of cylinders with small aspect ratios. However, the induced drag is underpredicted, especially for small drift angles. It is thus not suitable for the modeling of large ships with wind-assisted propulsion. Thus, in this study, wing theory for low aspect ratio wings is applied on ships sailing at a drift angle.

According to (Hoerner, 1985), the lift coefficient of a low aspect ratio wing ( $AR < 1$ ) is composed of a linear ( $c_{L1}$ ) and a nonlinear ( $c_{L2}$ ) part:

$$c_L = c_{L1} + c_{L2} \quad (29)$$

$$c_{L1} = \left(1 + \frac{\Delta b}{b}\right)^2 0.5 \pi AR \sin \beta \quad (30)$$

$$c_{L2} = k' \sin |\beta| \sin \beta \cos \beta \quad (31)$$

The term  $\left(1 + \frac{\Delta b}{b}\right)^2$  in equation (30) represents the decrease of the aspect ratio due to rounded edges of a low aspect ratio wing (Hoerner, 1985). For wings with a rounded plan form and rounded lateral edges, this might be set equal to 0.78 (Hoerner, 1985). The factor  $k'$  in equation (31) represents the cross flow drag coefficient (Hooft, 1996), which depends on the shape of the wing and can be compared to the cross flow drag coefficient described in (Hooft, 1996). It was argued in (Hoerner, 1985) that the 2D profile of the wing and the thickness ratio have a minor effect on the lift coefficient but that the main effect is from the planform and the shape of the edges, i.e., sharp or rounded edges. In (van der Kolk, 2016), it was discussed that  $c_{L2}$  is mainly dependent on the vortices created along the bilge of a ship and thus highly dependent on hull form features, such as bilge radius and the shape of the aftbody skeg. Using the measured lift coefficients of the three sample hulls, the factor  $k'$  is evaluated, and the results are shown in Fig. 13.

The calculated  $k'$  values in Fig. 13 decrease with increasing drift angle for hull 16 of the Delft series and the tanker, increase for the Series 60 and hull 19 of the Delft series, and is constant for hull 1 of the Delft series. An increasing  $k'$  value could motivate the linear part to be overpredicted and vice versa. However, from Fig. 13, no conclusions can be drawn about any dependency of the linear part on the ship's parameters, e.g., the Delft hull 16 and the Series 60 hull are very similar in aspect ratio, thickness ratio ( $B/L_{pp}$ ) and block coefficient but show the opposite behavior in Fig. 13. It should be noted that the Delft hull series does not have any aft body skeg; thus, the lateral area will increase with increasing block coefficient, which certainly will influence the lift and drag.

According to the theory presented in (Hoerner, 1985), the value of  $k'$  should highly depend on the shape and rounding of the edges, i.e., the

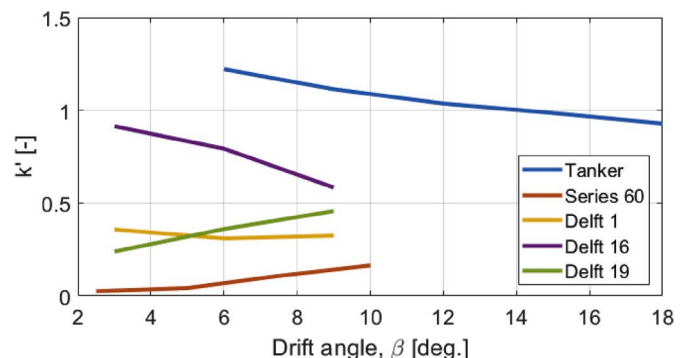


Fig. 13.  $k'$  value computed from measured lift coefficients.



bilge radius. If this would be the case for ships, it should be correlated to the block coefficient. Ships with low block coefficients have a higher bilge radius and should thus have a lower  $k'$  value. In contrast to this theory, the quadratic part of the side force can be determined according to (Inoue and Hirano, 1987):

$$Y_{vv} = 0.244 + 6.67 \left( (1 - c_B) \frac{T_D}{B} - 0.05 \right) \quad (32)$$

increasing with decreasing block coefficient. The mean value of the evaluated  $k'$  value from the model tests is shown in Fig. 14.

From these results, no dependency of  $k'$  on the block coefficient can be derived. Since it is not possible to detect a dependency of the value of  $k'$ , which is related to the cross flow drag, on any of the typical hull parameters, such as length to draft, length to beam, beam to draft or block coefficient, it must be concluded that the  $k'$  value highly depends on local hull form features, as discussed in (van der Kolk, 2016). Consequently, since the hull form is not mimicked in ShipCLEAN, the average value of  $k'$  shown in Fig. 14 is then used for the prediction of the side force:

$$c_L = c_{L1} + c_{L2} = 0.8 \cdot 0.5 \pi AR \sin \beta + 0.6541 \sin |\beta| \sin \beta \cos \beta \quad (33)$$

The  $k'$  value of 0.6541 is, as expected, much lower than the theoretical value of 2 for a flat plate (Hoerner, 1985). As it is presented in Fig. 14, the  $k'$  can differ significantly between different ships. This introduces uncertainties in the prediction of the drift angle. However, since the crossflow force is also included in the drag calculation using the same  $k'$  value (see Section 3.5.3), the lift to drag ratio is less affected. A comparison of the measured and the predicted lift coefficient is presented in Fig. 15a. The prediction according to equation (33) gives a 30% lower lift coefficient than the measurements for the Series 60 hull and a 50% higher value for the tanker, with the Delft series in between. However, for the performance prediction of wind-assisted ships, the resulting drift angle is of higher importance than the value of the generated side force. In Fig. 15b, a comparison of the drift angle during measurements and the drift angle that would generate the same lift according to the prediction are compared. The drift angles of all Delft hulls are very close, with a maximum of 1-degree deviation. The Series 60 hull shows a deviation of approximately  $2^\circ$  at the largest drift angle during measurements ( $10^\circ$ ), and the deviation for the tanker increases to  $3^\circ$ .

Keeping in mind the limited input to the ShipCLEAN model and the measurement uncertainties, these are acceptable prediction results, especially since the drag coefficient is coupled to the lift coefficient and not the drift angle (as described in the following section). To improve this method, more data is needed to find relations between the hull parameters, especially the bilge radius and block coefficient on (i) the  $k'$

value and (ii) the efficient aspect ratio, i.e., the factor  $\left(1 + \frac{Ab}{b}\right)^2$ .

### 3.6.3. Hydrodynamic drag forces of the hull

The prediction of the induced drag of the hull based on model tests or simulations is difficult since any uncertainties in the measurement of the longitudinal force will highly affect the induced drag, which, at small drift angles, is just a small part of the total drag force. With respect to this, the results from model tests must be handled carefully, and it must be expected that theoretical predictions will not accurately reflect all model test results.

As described in Section 3.5.2, the lift force consists of two parts, a linear part ( $c_{L1}$ ) and a nonlinear part caused by the cross flow drag ( $c_{L2}$ ). Subsequently, the drag must also be divided into two parts:

$$c_{Di} = c_{Di1} + c_{Di2} \quad (34)$$

The crossflow drag is a force acting normal to the ship's longitudinal axis, where the part normal to the inflow is considered as a lift force. The part parallel to the inflow is subsequently considered as drag:

$$c_{Di2} = k' \sin^3 |\beta| \quad (35)$$

Using the  $k'$  values shown in Fig. 13, the induced drag coefficient  $c_{Di1}$  is computed. In Fig. 16, the ratio of the potential lift coefficient ( $c_{L1}$ ) to the induced drag coefficient ( $c_{Di1}$ ) over the drift angle is presented. It must be noted that the presented lift to drag ratios are not the final values of the hull, since the corresponding parts of the crossflow force are added for both, the lift and the drag.

According to (Hoerner, 1985), the induced drag increases linearly with the drift angle and the potential part of the lift coefficient and can be computed by (with the drift angle  $\beta$  in radians):

$$c_{Di} = c_{L1} |\beta| a \quad (36)$$

where  $a = 0.5$  according to (Hoerner, 1985). Estimations of the values of factor  $a$  for the sample ships are shown in Fig. 17a. The value of  $a$  is larger than 0.5 for all hulls, and the drag coefficient is not linear to the drift angle. In Fig. 17b, the value of  $a$  for each hull is shown assuming that  $c_{Di}$  is proportional to  $\beta^{0.6}$ , which appears to be a better fit since the values of  $a$  are almost constant over the drift angle.

It can be observed that the hulls of the Delft series show a large spread of the estimated values of  $a$ . This implies that  $a$  is increasing with increasing block, midship or prismatic coefficient, since all other dimensions are equal for the hulls of the series. However, hull 1 of the Delft series ( $c_B = 0.72$ ,  $c_M = 0.942$ ,  $AR = 0.0471$ ) shows almost identical values of  $a$  as the Series 60 hull ( $c_B = 0.6$ ,  $c_M = 0.977$ ,  $AR = 0.0535$ ). Additionally, the tanker ( $c_B = 0.81$ ,  $c_M \approx 0.985$ ,  $AR = 0.0613$ ) shows smaller values of  $a$  than the Series 60 and the Delft hull 1, which contradicts the trends observed from the hulls of the Delft series. As mentioned in Section 3.5.2, the hulls of the Delft series do not have any aftbody skegs, which will cause additional effects since the lateral area will increase with increasing block coefficient.

As discussed in Section 3.5.1, the drag and lift coefficient might be affected by the wave pattern. A measure for the energy in the wave pattern, and thus the wave heights, is the wave resistance, i.e., the residual resistance of a hull. In Fig. 18, the mean values of  $a$  from Fig. 17b are related to the residual resistance coefficients ( $c_R$ ) of the hulls (estimated by ShipCLEAN). For the block coefficient, the Delft series hulls show an increasing trend of  $a$  with increasing  $c_R$ , while the group of the Series 60, Delft hull 1 and the tanker show the contrary.

In conclusion, with the available data, no clear dependency of the value of  $a$  on the block coefficient, the aspect ratio or the residual resistance coefficient can be found. Thus, the average value of  $a$  of all hulls is used, which appears to be close to the value proposed in (Hoerner, 1985), even though a linear dependency on the drift angle is assumed there.

In summary, the induced drag can be computed by:

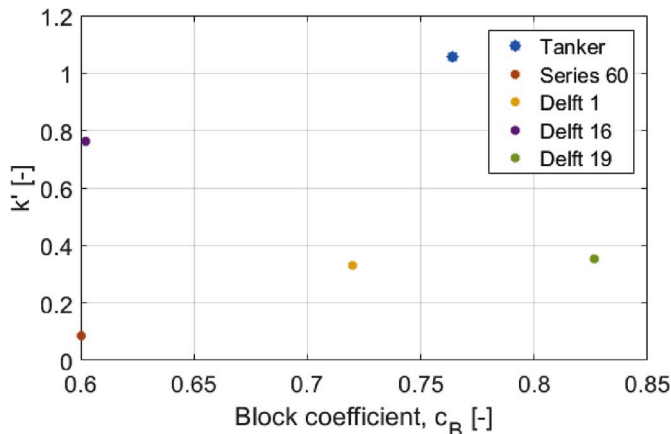


Fig. 14. Mean value of  $k'$  evaluated from model tests over the block coefficient.

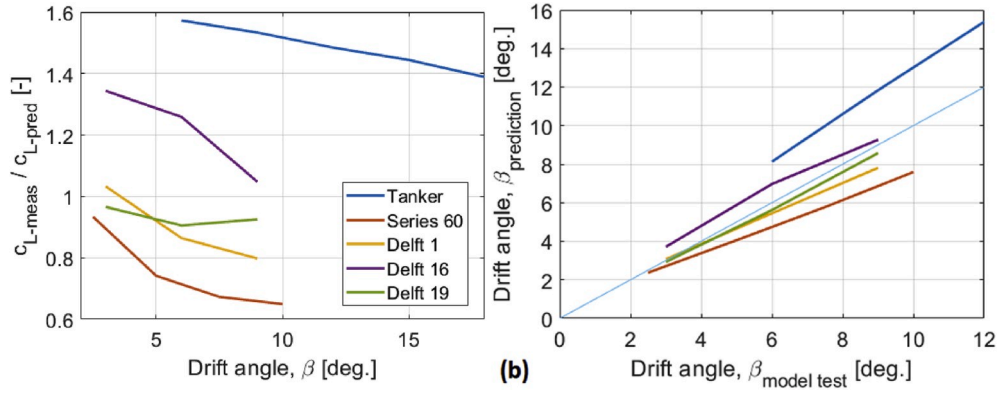


Fig. 15. Comparison of measurements (meas) and prediction (pred): (a) the lift coefficient and (b) the drift angle for equivalent lift.

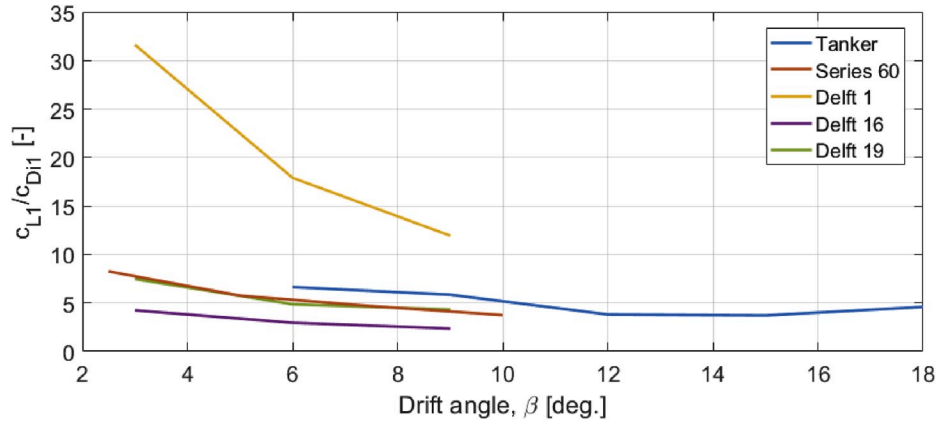


Fig. 16. Ratio of potential lift coefficient ( $c_{L1}$ ) to the induced drag coefficient ( $c_{Di1}$ ) over the drift angle.

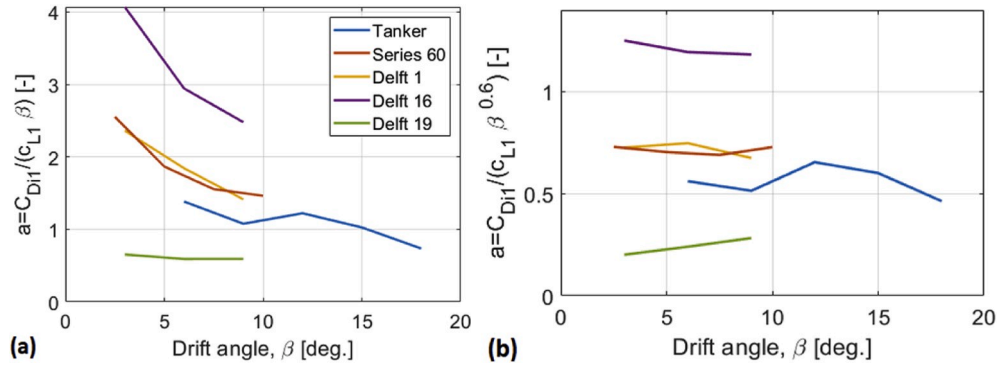


Fig. 17. Estimation of the value of  $a$  for (a) the linear case and (b) the nonlinear case.

$$c_{Di} = 0.66 c_L |\beta|^{0.6} + 0.6541 \sin^3 |\beta| \quad (37)$$

The lift-to-drag relation of all hulls is shown in Fig. 19 for the measured lift and drag (continuous lines) and the predicted lift and drag (dashed lines). Since the lift and drag coefficients proposed in this study only depend on the aspect ratio, all hulls of the Delft series will have identical coefficients.

Naturally, the largest deviation between the measured and predicted lift to drag is found for the Delft hulls 16 and 19. For the other hulls, the deviation of the lift to drag ratio is within 15%, which is deemed to be acceptable because of the limited input to the prediction and the limited measurement data available. With more measurements or simulations, a relation between the hull parameters (especially the block coefficient) and the factor  $a$  might be found. Additionally, local hull form features,

especially the bow, i.e., the leading edge, will have considerable effects on the drag force.

#### 3.6.4. Center of effort of the hydrodynamic lift force

Accurately predicting the center of effort of the lift force is crucial to predicting the necessary rudder angle. The center of effort of the crossflow and the potential part of the lift force are at the geometric center of the lateral area (Kume et al., 2006), and close to the center of the low pressure in the bow region (Abbott and Von Doenhoff, 1959), respectively. Additionally, the pressure distribution with low pressures at the forward downstream side and aft upstream side and high pressures at the forward up stream and aft downstream side, creates a moment that tends to rotate the ship broadside to the flow. This moment is also called the Munk moment (Lewandowski, 2004). Since it is not

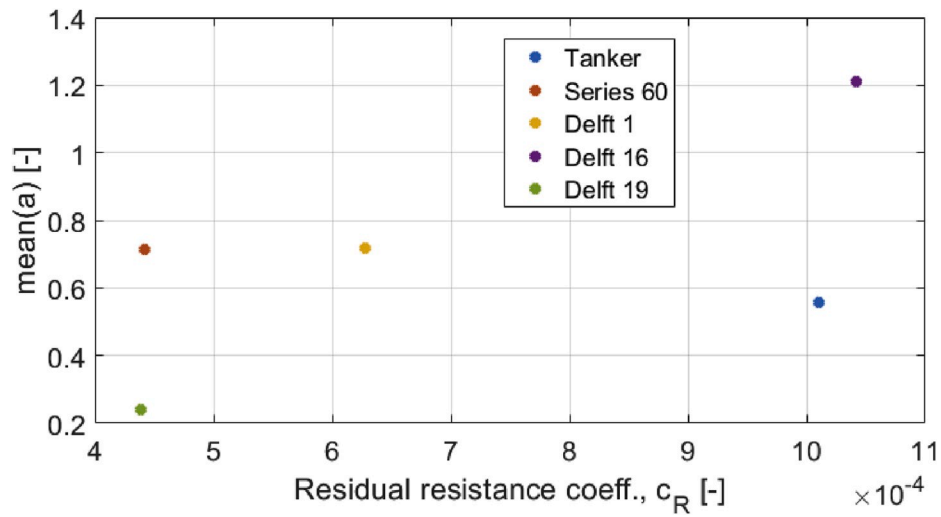
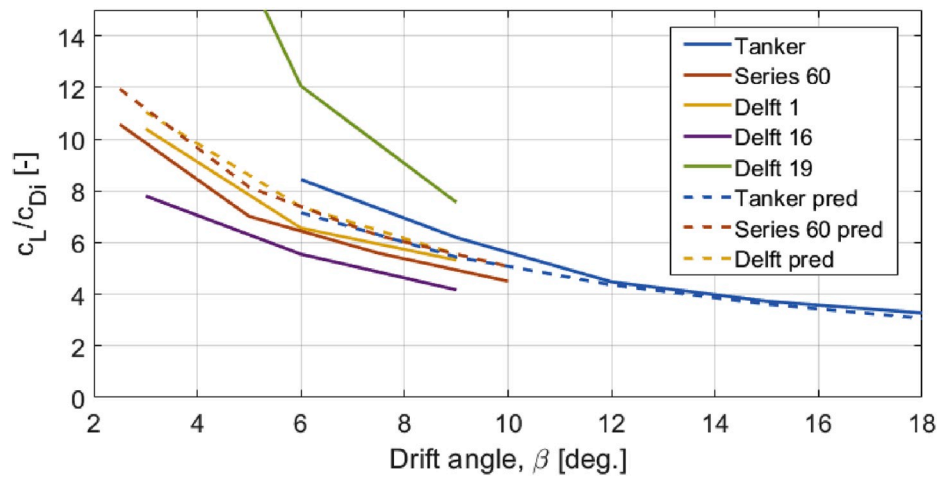
Fig. 18. Mean value of  $a$  over the residual resistance.

Fig. 19. Lift to drag ratio according to measurement (solid lines) and from predictions (dashed lines).

possible to calculate the value of the Munk moment without CFD computations, it is included in the estimation of the center of the lifting force. However, empirical methods for maneuvering predictions, as in (Inoue and Hirano, 1987), include the Munk moment in the prediction of

the yaw moment. The Munk moment is also the cause that some ships experience force centers well ahead of the ship, as for example reported in (van der Kolk et al., 2019b).

For a 2D wing, the center of effort of the lift force, including the

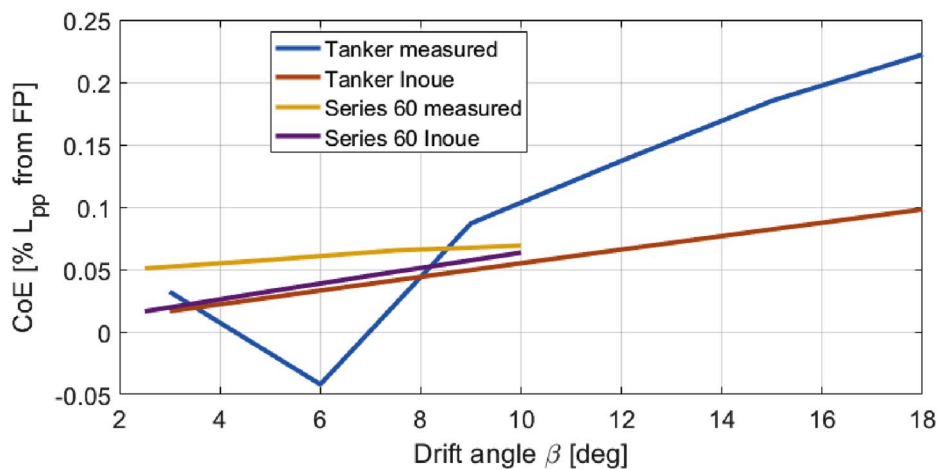


Fig. 20. Measured and predicted center of effort for the tanker and the Series 60.

Munk moment, is approximately 25% of the chord length from the tip, and the center of effort moves towards the leading edge for 3D wings with decreasing aspect ratios (Abbot and Von Doenhoff, 1959). Since the aspect ratios of ships are very small, the center of effort should be close to the bow. The measurement results of the Series 60 and the tanker prove this statement. However, the results from the Delft series indicate that the center of effort is in front of the hull, by up to a full ship length. However, the Delft hull series is rather special since the hulls do not have any form of skeg in the aft; thus, the center of the lateral plane is far forward (compared to the other hulls).

In Fig. 20, the measured center of effort of the Series 60 and the tanker are compared with the predicted center of effort from the method proposed in (Inoue and Hirano, 1987). Although the prediction does not fully match the measured values, the trend of a more aft position of the center of effort with increasing drift angle is captured. Since both, the side force and the yaw moment are small in model tests, the calculated center of effort from model test results can deviate from reality. In ShipCLEAN, the center of effort is predicted using the equations proposed in (Inoue and Hirano, 1987):

$$CoE = \frac{N_h}{Y_h} L_{PP} = \left( \frac{N_v}{Y_v} \sin|\beta| + \frac{N_{vv}}{Y_{vv}} (\sin|\beta|)^2 \right) L_{PP} \quad (38)$$

$$N_v = 2 \frac{T}{L_{pp}} \quad (39)$$

$$N_{vv} = 0.066 - 0.96 (1 - c_B) \frac{T}{B} \quad (40)$$

$$Y_v = \pi \frac{T}{L_{pp}} + 1.4 c_B \frac{B}{L_{pp}} \quad (41)$$

$$Y_{vv} = 0.244 + 6.67 \left( (1 - c_B) \frac{T}{B} - 0.05 \right) \quad (42)$$

### 3.6.5. Lift and drag of high aspect ratio centerboards

To increase the hydrodynamic side force generated by the ship, the addition of center- or daggerboards is an efficient possibility. To achieve high lift to drag ratios, these centerboards must be high aspect ratio wings, i.e.,  $AR > 4$ . The lift and drag coefficients of a high aspect ratio wing can be computed by (Houghton et al., 2017; Hoof, 1996):

$$c_L = \frac{2\pi}{1 + 2/AR_E} \sin \beta \quad (43)$$

$$c_D = c_{D0} + \frac{c_L^2}{\pi AR_E} \quad (44)$$

$$c_{D0} \approx 0.005 - 0.01 \quad (45)$$

In equations (43) and (44),  $AR_E$  denotes the efficient aspect ratio:

$$AR_E = k AR \quad (46)$$

If the centerboard is mounted to a flat surface that is at least as wide as the centerboard chord length,  $k$  can be assumed to be set to 2 (Abbot and Von Doenhoff, 1959).

## 4. Design and operation of wind-assisted ships

This section presents examples of cases that refer to ship operations, retrofitting and new designs of wind-assisted ships. The purpose is to demonstrate the usability of the ShipCLEAN model and how it can be used as a powerful simulation tool to analyze, compare and recommend the design and operation of wind-assisted ships. Section 4.2 discusses different modes of operation, i.e., control of the rotor's rpm. In Section 4.3, the optimal placing and number of rotors are discussed, followed by analyses of specific design recommendations for wind-assisted propulsion. Section 4.4 discusses changes of the hull form, propeller and

general ship design if a ship is designed from scratch to have wind-assisted propulsion. Uncertainties in the prediction of fuel savings from the Flettner rotors are discussed in Section 4.5.

Two ships, a two-propeller, open-shaft RoRo and a conventional single-skeg tanker with main dimensions according to Table 2, are used as case study ships. The dimensions and costs of the Flettner rotors are shown in Table 3 based on data in (Norsepower, 2019b).

Initially, both ships are equipped with four rotors, as shown in Fig. 21. These initial configurations are used for the studies in Section 4.2. The rotors are arranged to not interfere with the superstructure or the cargo area of the ships. For the faster, twin-propeller (and rudder) RoRo, the rotors are placed further aft, since the ship has a forward superstructure and the double rudders can take more side force loads.

Polar plots of the fuel consumption per nautical mile (nm) with sails related to the fuel consumption per nm without sails are shown in Fig. 22 for a TWS of 10 m/s and a ship speed of 12 kn for the tanker and a ship speed of 18 kn for the RoRo. With this wind speed and a TWA less than 40–50 degrees off bow, the sails create added fuel consumption. However, the sails can generate fuel savings of up to 65% for the tanker and 55% for the RoRo. For both ships, the maximum savings are at a TWA of approximately 110°. The power consumption of the rotors is included in the remaining propulsion power and thus affects the fuel consumption. The maximum rotor power is about 100 kW for a single  $5 \times 30$  m Flettner rotor. For the ships with 4 Flettner rotors this corresponds to a maximal power consumption of the rotors of about 5% of the calm water propulsion power of the RoRo at 18kn and about 15% of the calm water propulsion power of the tanker at 12 kn.

### 4.1. Weather conditions and method to evaluate the expected savings

Wind measurements from ships on two routes, one on the Pacific Ocean and one on the Baltic Sea, are available from reference vessels in the ShipCLEAN project. These measurements are used to simulate and assess the performance of the wind-assisted ships for several scenarios. The tanker is evaluated with the measurements from the Pacific Ocean and the RoRo with the weather from the Baltic Sea. Measurements were taken every hour, over a full year. A total of 6600 measurements with ship speeds higher than 5kn were taken for the Pacific Ocean route (up time of 76%), and 4700 measurements with ship speeds higher than 5kn were taken for the Baltic Sea route (up time of 54%).

Wind “rose” plots of the measured TWA and TWS on the Pacific Ocean (a) and the Baltic Sea (b) are presented in Fig. 23. Although ShipCLEAN can simulate asymmetric rotor arrangements, the current study is limited to symmetric arrangements of the rotors. Thus, the wind angles are shown only for 0–180° TWA. With a peak at approximately 90–140°, the wind angles on the Pacific Ocean route are much more favorable than on the Baltic Sea route, which shows a peak at approximately 10–80°. For both routes, the wind speeds are distributed equally, independent of the wind angle.

To save computational time, a weighting system for different wind angles and speeds is developed. The goal is to evaluate a set of 4 polar diagrams in steps of 20° for each ship (a total of 40 points per ship, at operational speed). The simulations were performed for one target speed and account for involuntary speed loss, i.e., reduced speed if the

**Table 2**  
Main particulars of the two case study vessels.

	RoRo	MR tanker
$L_{oa}$ [m]	200	183
$B$ [m]	27.0	32.2
$T$ [m]	6.5	11.0
$\Delta$ [t]	21 000	50 600
$v_{des}$ [kn]	20	15
$v_{service}$ [kn]	18	12
Deck height [m]	11.0	4.2
$GM_0$ [m]	1.0	4.4



**Table 3**

Dimensions, initial costs and maintenance costs of the Flettner rotors in this study.

Height [m]	30
Diameter [m]	5
Height of base [m]	3
Weight (incl. foundation) [t]	59
Initial investment per unit [EUR]	750 000
Yearly costs per unit [EUR]	15 000
Max. wind speed for operation [m/s]	20

required power and rpm are outside of the engine envelope (Tillig et al., 2017). The fuel savings at each angle will be multiplied with a weighting for the TWA, and the sum of all savings at one TWS will then be multiplied by a factor for the wind speed. With this procedure, described in more detail later in this section, it is possible to predict the expected fuel savings on the routes without evaluating each single measurement point. However, all points will be simulated for the ships without sails to obtain a benchmark fuel consumption to predict the payback times of the rotors.

To evaluate the weights, probability density distributions (pdf) are fit to the measurement data. Histograms of the measurement data and the pdfs are presented in Fig. 24 for the TWA and Fig. 25 for the TWS. Weibull distributions are used for the TWS data, and Kernel distributions are used for the TWA data. The weights are evaluated by:

$$w = \frac{\int_{x_1}^{x_2} pdf \, dx}{\int_0^{x_{max}} pdf \, dx} \quad (47)$$

The resulting weights for the selected TWA and TWS ranges are shown in Table 4 and Table 5, together with the TWA and TWS that are used for estimating the fuel savings for the TWA and TWS range (TWS<sub>C</sub>, TWA<sub>C</sub>). The expected fuel savings are computed as the weighted sum of the estimated savings in all TWS and TWA combinations.

For the ships without and with sails, the difference between the fuel consumption evaluated with all points of the route and the fuel consumption evaluated with the above method is 2.2% and 2.7% for the tanker and 3.1% and 3.3% for the RoRo, respectively. Considering that the power difference caused by an increase of the wave height from 3 to 4 m is about 19% for the RoRo and 34% for the tanker, these differences are smaller than what could be expected between different years due to different weather conditions. The above described method thus proved to be suitable for predicting fuel savings with acceptable accuracy for

the purpose of the simulations and analyses. An even more accurate prediction of the long-term fuel savings could be achieved by increasing the time span of the measurements from 1 year to multiple years. However, for this study the time span of the measurements was limited to one year.

The wave heights are computed according to equations (48) and (49) (Coastal Engineering Resea, 1984), with a maximum fetch of 50 nm for the Baltic Sea and 300 nm for the Pacific Ocean. The wave encounter angle is assumed to be equal to the TWA. This assumption introduces uncertainties (see Section 4.5) since neither geographical effects (e.g. land protection and shallow water), or swell waves caused by weather systems further away are respected in the wave height estimation.

$$H_s = 0.01616 U_A \sqrt{\text{fetch}} \quad (48)$$

$$U_A = 0.71 \text{ TWS}^{1.23}, \text{ TWS in [m/s]} \quad (49)$$

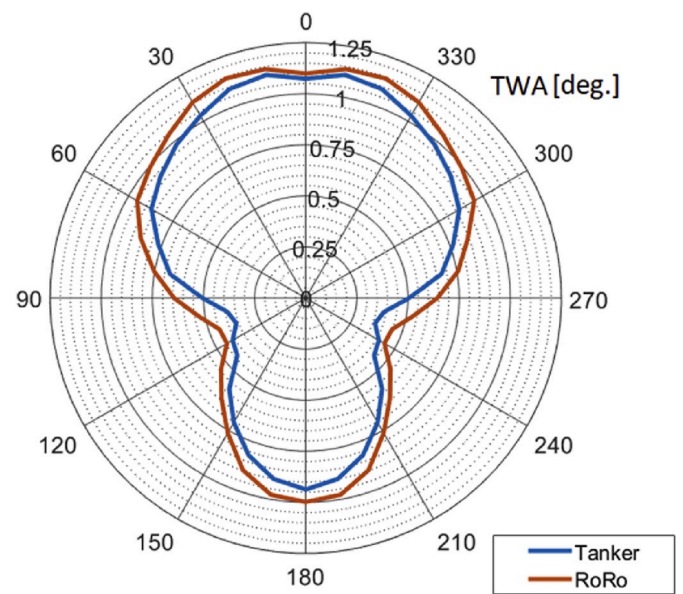
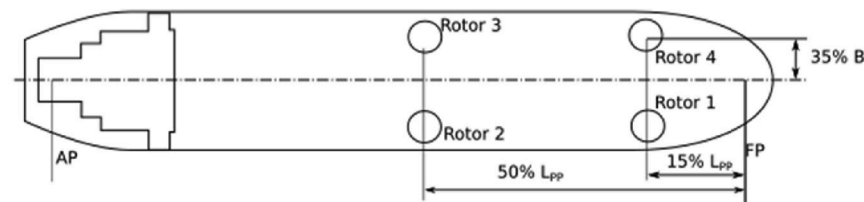


Fig. 22. Relative (with/without sails) fuel consumption per nm for the initial setups as function of the TWA, TWS = 10 m/s,  $v_s = 12$  kn (tanker), 18 kn (RoRo).

## Tanker



## RoRo

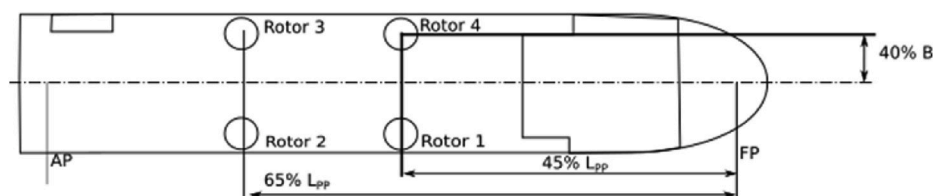


Fig. 21. Initial position of the Flettner rotors on the tanker (top) and the RoRo (bottom).

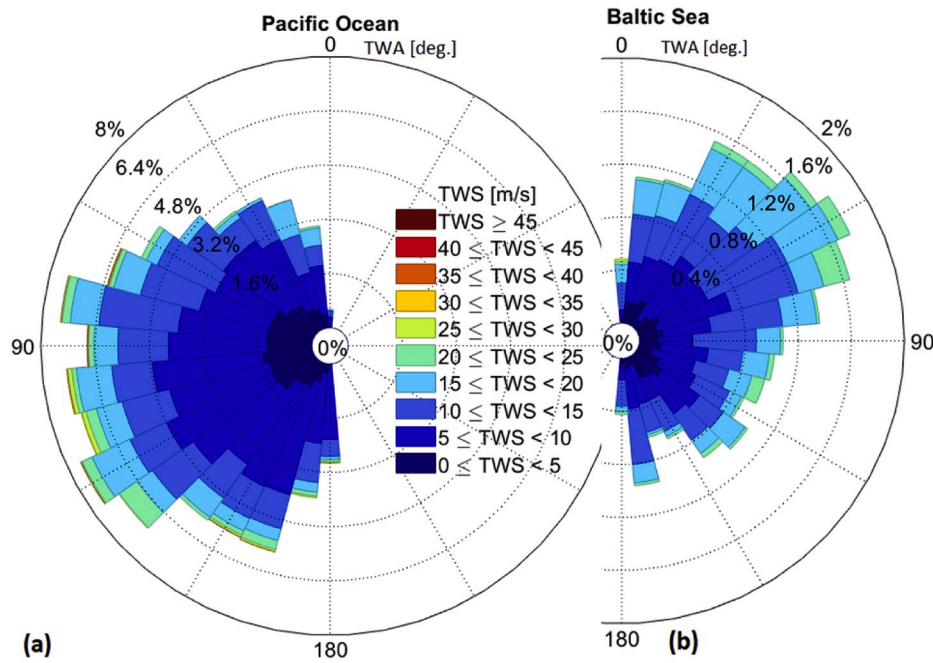


Fig. 23. Wind rose plots of the true wind speed and angle on (a) the Pacific Ocean and (b) the Baltic Sea.

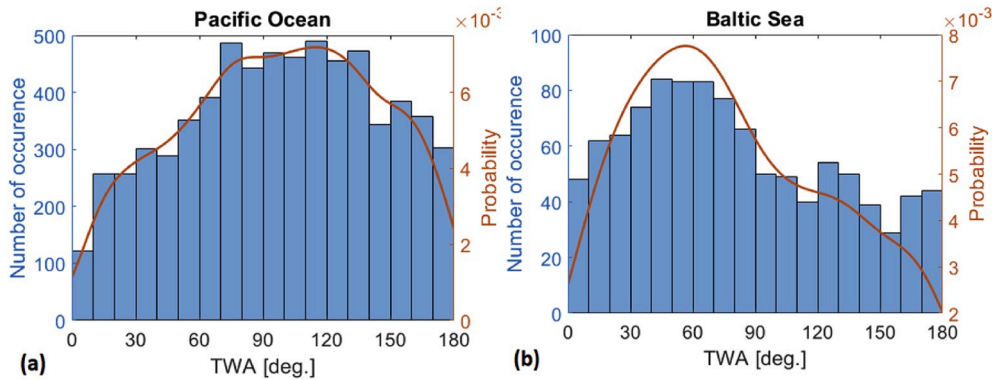


Fig. 24. Histogram of measured TWA with fitted distribution for (a) the Pacific Ocean and (b) the Baltic Sea.

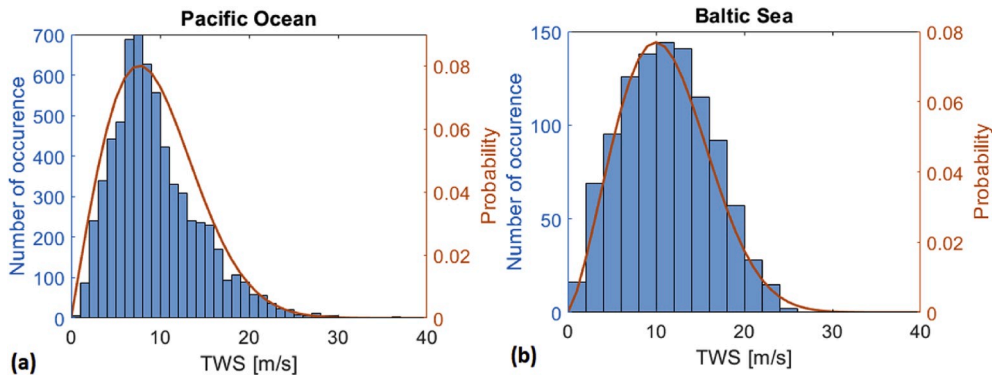


Fig. 25. Histogram of measured TWS with fitted distribution for (a) the Pacific Ocean and (b) the Baltic Sea.

#### 4.2. Operation

Two main problems exist in the operation of wind-assisted propelled ships using Flettner Rotors: (i) choosing the optimal rpm of the rotors and (ii) choosing the optimal course/wind angle to minimize the fuel

consumption with constant velocity made good (VMG). While the second, optimal wind angles, is similar for other sail types, the first problem is ultimately about choosing the optimal angle of attack of the sails. The importance of an efficient rpm control is discussed in (Bordogna et al., 2020). In (Bordogna et al., 2020) it is shown that possible negative

**Table 4**

Weights for TWA ranges.

Range [deg]	0–10	10–30	30–50	50–70	70–90	90–110	110–130	130–150	150–170	170–180
TWA <sub>C</sub> [deg]	0	20	40	60	80	100	120	140	160	180
W <sub>RoRo</sub>	0.036	0.118	0.153	0.162	0.139	0.109	0.097	0.087	0.072	0.027
W <sub>tanker</sub>	0.019	0.073	0.093	0.116	0.140	0.140	0.146	0.128	0.106	0.035

**Table 5**

Weights for TWS ranges.

Range [m/s]	0–5	5–10	10–15	15–20	>20
TWS <sub>C</sub> [m/s]	2.5	7.5	12.5	17.5	22.5
W <sub>RoRo</sub>	0.104	0.333	0.341	0.171	0.051
W <sub>tanker</sub>	0.188	0.386	0.282	0.112	0.031

interaction effects between rotors can be highly reduced with a rpm control.

#### 4.2.1. RPM control of Flettner rotors on a ship

If the interaction between the sails and the hull is neglected, i.e., drift and associated induced resistance and heel, the optimal rpm of the Flettner rotors is determined by maximizing the net power, as shown in equation (10). However, since interaction must be considered, the rpm of single or several rotors (sails) must be reduced in certain conditions, hereafter called “reefed”. The sails must be reefed in case at least one of the following conditions is true:

1. The heel angle is larger than the allowed maximum (in ShipCLEAN  $\phi_{\max} = 8^\circ$ ).
2. The rudder angle is larger than the allowed maximum (in ShipCLEAN  $\delta_{\max} = 10^\circ$ ).
3. The sails cause resistance instead of a forward thrust.
4. The induced resistances from the rudder and hull drift are reduced more than the sail thrust if the sails are reefed, i.e. the rpm of one or several rotors is reduced.

Cases 1–3 can be identified from the 4 DOF solution, and case number 4, i.e., that the additional drag reduces quicker than the sail thrust, can only be investigated by comparing a reefed and non-reefed condition. However, case 4 is the most important for achieving the maximum efficiency of the sails, especially in apparent wind angles forward from abeam.

For case number 3, i.e., the sails causing resistance instead of thrust, all sails are put into idle mode, i.e., the rpm at which the drag is minimal. The minimum drag is found to be at a spin ratio of approximately 0.5 (Li et al., 2012; Kramer et al., 2016). In all other cases, only the most suitable rotors should be reefed to achieve the best possible balance between hull drift and rudder angle by moving the center of effort of the sail forces. From analyzing the formulation for the lift and drag of the rudder (equation (23) and (24)) and the hull (equation (33) and (37)), it can be found that the lift to drag ratio of the rudder is much higher than the lift to drag ratio of the hull. Thus, to minimize drag, as much of the required lift force as possible must be delivered from the rudder. For all conditions with side forces equal to or higher than the lift force of the rudder at the maximum angle, the maximum rudder angle will be optimal. Three different conditions must thus be defined to specify which rotor to reef:

1. The rudder angle is close to the optimal angle.
2. The rudder angle is smaller than the optimal angle.
3. The rudder angle is larger than the optimal angle.

For condition 1, all rotors are reefed simultaneously to keep the yaw moment as constant as possible. For conditions two and three, a score system is employed. The score system assumes that the first rotors to reef

are those with a low thrust to side force ratio; thus, those rotors obtain low scores. Additionally, a score is added for the yaw moment. For condition 2, rotors with a low yaw moment obtain low scores, since the rudder angle, i.e., the yaw moment, will be larger. For condition 3, rotors with high yaw moments obtain low scores. In all cases, reefing is performed iteratively, with reefing factors evaluated from the required difference in side force or yaw moment. The fuel savings with and without rpm control in 10 m/s TWS are presented in Fig. 26 for the tanker (a) and the RoRo (b). It is obvious that rpm control is crucial to maximize savings and avoid added consumption in TWA between 30 and 80 degrees off bow. Using the method described in Section 4.1, the estimated fuel saving for the RoRo with the initial sail set up and the rpm control is 14.3%; without the rpm control, this drops to 12.0%. For the tanker, the fuel savings are 26.0% with the rpm control and 24.8% without.

In Fig. 27, the rpm of each rotor is presented for the tanker (a) and RoRo (b). It must be kept in mind that a low rpm is not always the result of reefing but might be due to lower local wind speeds or different wind angles. The results from the RoRo show that the full sail power, i.e., all sails at full rpm, is only used at a TWA more than 110 degrees off bow. It must be concluded that, even if the sails produce thrust in wind angles more than 30 degrees off bow, it is not beneficial to run all sails with full rpm in all conditions.

#### 4.2.2. Optimal TWA

In Fig. 22, the fuel savings are highly dependent on the TWA. Thus, it can be assumed that it is beneficial to divert from the direct course to sail at more favorable TWA while increasing the speed to keep the velocity made good (VMG) constant. The speed at the new course can be computed by (with TWA<sub>init</sub> as the TWA on the direct course):

$$v_S = v_{S_{init}} / \cos(TWA - TWA_{init}) \quad (50)$$

In Fig. 28, the fuel consumption per hour related to the fuel consumption on the direct course is shown for 3 diversion angles and 5 initial TWAs. While there are no fuel savings if the TWA on the direct course is  $0^\circ$  (headwind), the gains at an initial TWA of  $80^\circ$  can reach 30%. It must be noted that the results do account for increased ship speed due to the longer distance travelled, but do not account for any necessary tacking or different wind angles further into the journey in order to reach the destination. Naturally, the results for the complete journey highly depend on the weather ahead. The achievable fuel savings and the dependency of the results on the weather along the route show the necessity of sophisticated weather routing for wind-assisted ships.

#### 4.3. Retrofit

The focus in this section, as part of a retrofit project, is on the optimal size and number of sails and on the optimal position of the sails. Before varying the position of the sails, 7 different arrangements are evaluated for the tanker and 4 different arrangements are evaluated for the RoRo; see Fig. 29. The arrangements are designed and chosen to have similar geometric centers of the array of rotors.

The ShipCLEAN model with wind-assisted propulsion was used to make simulations and analyses of the fuel savings for each of the cases. The results are shown in Fig. 30a for the 7 rotor arrangements on the tanker, using the Pacific Ocean route and Fig. 30b for the 4 rotor arrangements on the RoRo, using the Baltic sea route. Additionally, the



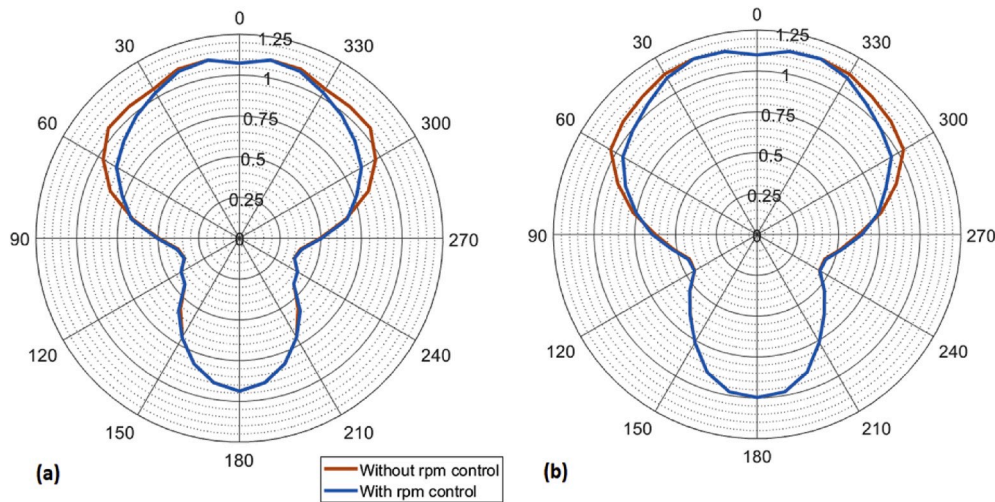


Fig. 26. Comparison of fuel savings as a function of the TWA (saving: less than unity) with and without rpm control for (a) the tanker and (b) the RoRo.

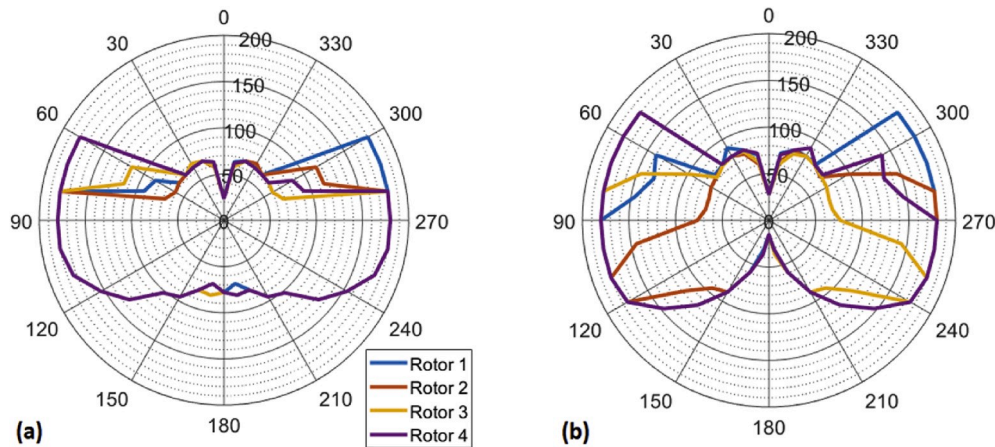


Fig. 27. RPM of the rotor sails in 10 m/s TWS as a function of the TWA, for (a) the tanker and (b) the RoRo.

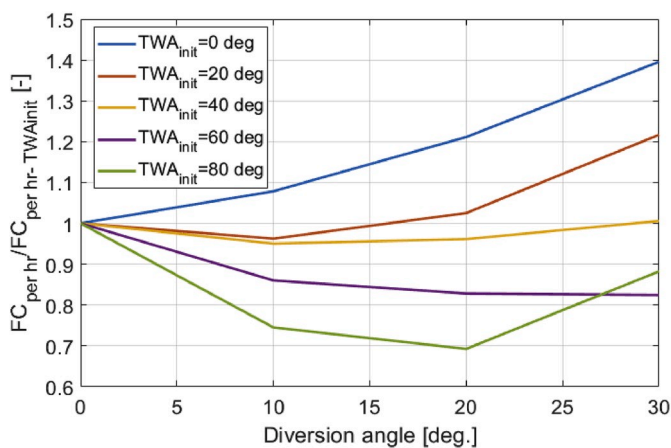


Fig. 28. Relative fuel consumption per hour at different TWAs with constant VMG for different diversion angles.

payback times are estimated for 3 different fuel prices, 300 EUR/ton, 500 EUR/ton and 700 EUR/ton. The results from this economic analysis are shown in Fig. 31a for the tanker and Fig. 31b for the RoRo.

The results show that, compared to the ships without wind-assisted propulsion, fuel savings greater than 30% can be achieved for the

tanker. Savings for the RoRo are found to reach 14%. Since the fuel savings do not increase linearly with the number of rotors (due to headwind and reefing) but the investment and maintenance costs do, the payback time is found to be the shortest for the arrangements with the fewest sails. Comparing the results from arrangements T4.1, T4.2, T6.1, T6.2, R2.1 and R2.2, it becomes obvious that due to interaction effects between the rotor sails, it is important to choose the optimal arrangement for a given number of rotors. However, it must be kept in mind that the positions of the rotors in this study are not fully optimized for those arrangements.

The two most promising arrangements (the one with the shortest payback time and the one with the highest savings) per ship are chosen for further variation of the rotor's position. The variables for variation are the longitudinal positions of the rotors. During the variation, a minimal distance between the rotors of 10% of the ship's length is ensured. The best variants from this study are presented in Table 6, with the fuel savings from the initial positions shown within brackets. The results show that the savings are larger if the rotors are arranged further aft, i.e., if the side force on the rudder is higher. How far aft the rotors can be arranged depends on the size of the rudder and the speed of the ship, i.e., the maximal side force the rudder(s) can produce. Due to the double rudders and higher speeds of the RoRo, the best arrangement for this ship is when the aft rotors are almost above the rudder.



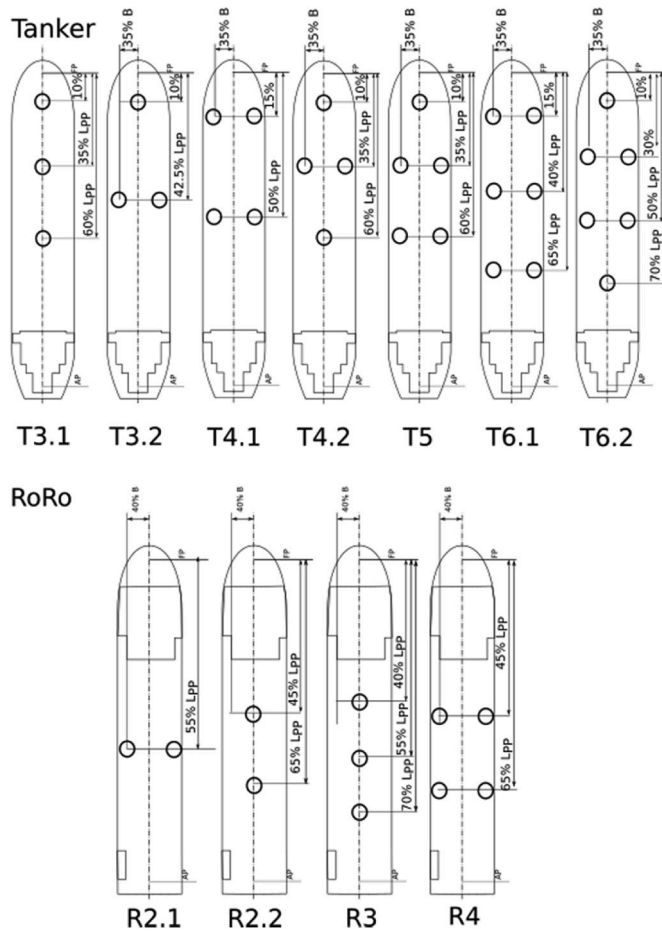


Fig. 29. Sail arrangements for the tanker (top) and the RoRo (bottom).

#### 4.4. New design

From the result with the two example ships and the theory in Section 3, it can be concluded that if the superstructure is short and the deck is free, the focus during a new design project for wind-assisted ships should be on the hydrodynamics. With high side and thrust forces from the sails, there are two areas of interest for improvement of hydrodynamics of wind-assisted ships: (i) the propeller design due to varying thrust load and (ii) the hydrodynamic lift generation, since the side force from the

sails must be compensated.

The first area, the propeller design, addresses avoiding pressure side cavitation, which occurs at low propeller loads, i.e., when the sails produce a considerable amount of forward thrust. Since the sails contribute up to 100% of the necessary thrust, there will be conditions when the propeller is windmilling. For the tanker with the T6.1 sail arrangement, the propeller loadings are between 0% and 125% of the propeller loadings without sails. Due to those variable propeller loadings, it must be concluded that ships designed for wind-assisted propulsion, i.e., with considerable large sail areas, must be equipped with a controllable pitch propeller to avoid pressure side cavitation.

To increase the hydrodynamic lift generated by the hull, the hull form should be designed accordingly. In equation (33), it is shown that the generated lift is linearly dependent on the aspect ratio of the hull; thus, wind-assisted ships should be designed with the highest AR possible, i.e., high draft and short length. However, decreasing the length will increase the resistance. As shown in Section 3.5, there are differences in the lift and drag coefficients of the hulls studied that could not be captured by the wing theory, which indicates that the hulls of wind-assisted ships must be evaluated at a drift angle already in the design stage. However, even the hulls with the best lift to drag ratio are considerably worse than wings with high aspect ratios. Thus, the most efficient way to increase the lift to drag ratio is to increase the area of any high aspect ratio wings on the hull, i.e., the appendages. For typical hulls, this is only the rudder(s). One consideration could thus be to design the ships with twin rudders, even if the ship is a single-propeller design. Furthermore, center- or daggerboards could be applied to the hull, as discussed in Section 3.5.5.

To show the effect of centerboards and double rudders, the tanker and RoRo examples are modified. The tanker is fitted with double rudders, i.e., the rudder area is doubled, and a centerboard. The double rudders are not placed in the propeller slipstream, which reduces the rudder forces. This effect is captured in ShipCLEAN. For the RoRo, two daggerboards are fitted that are designed to keep the draft below 10 m, i.e., suitable for the Baltic Sea, while the centerboard of the tanker is designed to be theoretically fully hoistable into the hull. The position of the centerboard is chosen slightly forward of the geometrical center of the sails. The dimensions of the applied dagger-/centerboards are shown in Table 7. The tanker is tested with the T6.1 rotor arrangement, and the RoRo is tested with the R4 arrangement.

For the tanker, the centerboard and double rudders increase the savings from 32.1% to 36.1%, and for the RoRo, the savings increase from 14.3% to 16.8%. The results show that centerboards can increase the efficiency of a wind-assisted propelled ship. However, to achieve maximum savings, the side force distribution between the hull, the

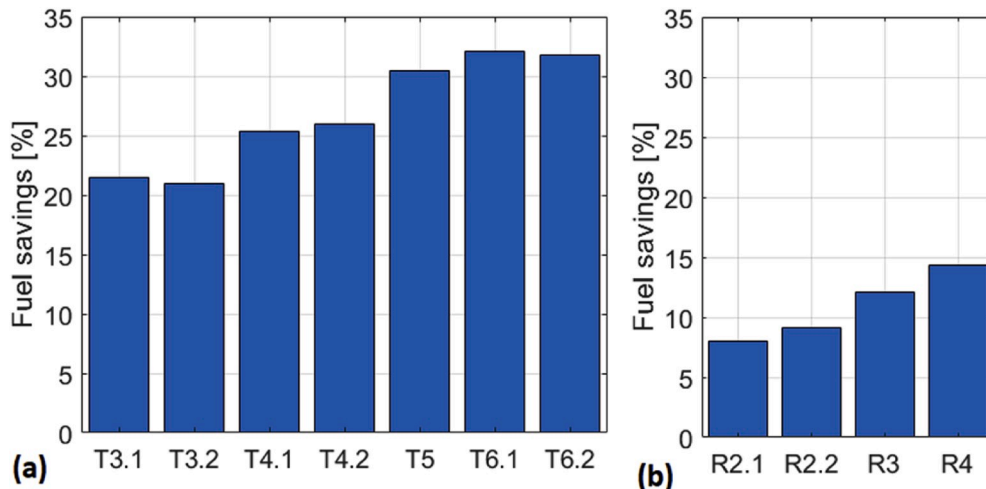


Fig. 30. Fuel savings with different Flettner rotor arrangements for (a) the tanker and (b) the RoRo.

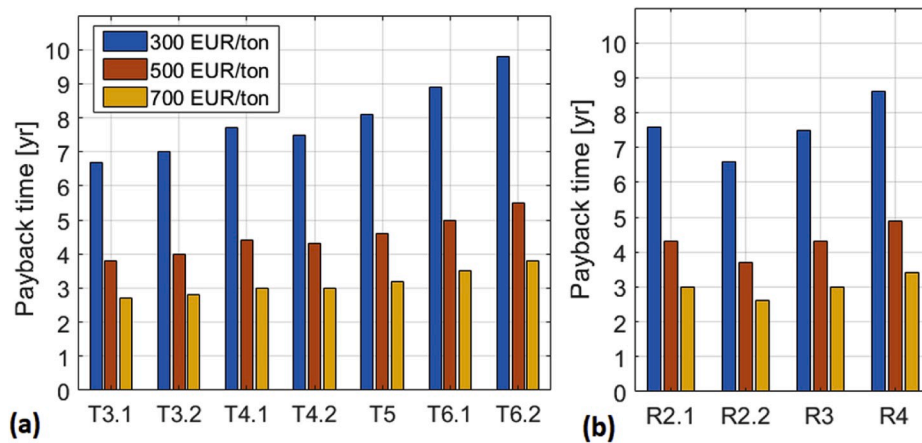


Fig. 31. Payback times for the different rotor arrangements and three different fuel prices (300, 500, 700 EUR/ton) for (a) the tanker and (b) the RoRo.

Table 6

Results from optimizing the longitudinal positions of the rotors.

	Best position [% $L_{pp}$ ]	Fuel saving [%]
T3.1	20, 45, 70	23.1 (21.5)
T6.1	25, 45, 70	36.0 (32.1)
R2.2	60, 90	12.5 (9.1)
R4	60, 90	21.1 (14.3)

rudder and the centerboard must be optimal. This requires the centerboard position to be optimized together with the sail arrangement and position.

#### 4.5. Uncertainties in the prediction of fuel savings from wind-assisted propulsion

This section presents a discussion of the uncertainties in the prediction of fuel savings from wind-assisted propulsion. It must be noted that this is a qualitative discussion of the uncertainties but not a complete, quantitative, uncertainty study. Especially for the full-scale sail forces, drift forces and aerodynamic interaction effects, more measurement data must be available to quantitatively evaluate the uncertainties.

Uncertainties in the prediction of the fuel consumption and fuel savings with wind-assisted propulsion can be divided into four parts: (i) uncertainties in the prediction of the hull resistance, propulsive efficiency and specific fuel oil consumption of the engine, (ii) uncertainties in the prediction of the sail forces, (iii) uncertainties in the prediction of the hydrodynamic lift and drag of the hull, and (iv) uncertainties in the prediction of the encountered weather.

The uncertainties in the power prediction using ShipCLEAN are quantified in (Tillig et al., 2018). However, since only fuel savings are of interest in this study, these uncertainties will not affect the results since the resistance and propulsive efficiency are similar for the ship with and without wind-assisted propulsion. Since the payback time depends on the total fuel costs, it will be influenced by the uncertainties quantified in (Tillig et al., 2018).

The sail forces of a single rotor were verified against full-scale

measurements with good agreement for the lift, drag and power coefficients, see Section 3.5. The comparison of the lift coefficient in a typical operational range of spin ratios between  $SR = 1.5$  and  $SR = 2.5$  shows that the difference between the full-scale measurements and the ShipCLEAN prediction are less than 0.2% and the difference to the values according to (Li et al., 2012) is less than 4%. A similar comparison for the drag coefficient shows a difference of less than 1% for the ShipCLEAN predictions, which is in agreement with the values in (Li et al., 2012). The predicted power coefficient is within 1% of the mean value of the measurements, for the given SR range. The above differences show that the expected uncertainty in the prediction of the sail forces and power consumption for a single rotor is most likely well below 4%.

The prediction of the aerodynamic influences was compared to model test results (see Section 3.5) and it was shown that the predictions and the measured trends of the thrust forces were similar. Larger differences were found for the side forces. However, a quantification of uncertainties based on this comparison is not possible since the rotors were of different geometry and showed different lift and drag coefficients in single rotor tests. However, the influence of the aerodynamic interaction on the total thrust is small if the rotors are operated at their optimal SR for the local wind speed and direction, as discussed in Section 3.3. Larger differences were found for the longitudinal center of the sail forces. It is thus concluded that the uncertainty of the prediction of the fuel savings related to the aerodynamic interactions is small. However, uncertainty in the optimal positions of the rotors might be considerable.

The largest model uncertainties are expected from the lift and drag force prediction of the hull sailing at a drift angle. In Section 3.5.2, it is discussed that the predicted drift angle shows a difference of  $1-3^\circ$  (at approximately 10 degrees of drift) compared to the model tests of the sample ships. However, a difference of  $1-3^\circ$  in drift angle only results in a maximum difference of sail thrust (due to the change of TWA) of approximately 1%. Thus, more emphasis is put on an accurate prediction of the lift to drag ratio of a ship. In Section 3.5.3, it is evaluated that the predicted drag force differs by approximately 15% from the measured drag force during model tests of the sample ships. For the tanker and the RoRo with the sail arrangements T4.1 and R4, the average of the predicted drag force is approximately 8% of the calm water resistance. Thus, for these sail arrangements, the uncertainty of the fuel saving prediction due to the uncertainty of the drag force can be estimated to approximately 2%. These results show that the accuracy of the drift angle prediction, i.e. the prediction of the lift force is not as important as the accurate prediction of the lift to drag relation of the hull.

Large uncertainties are related to the prediction or variation of the weather conditions the ship will experience during its voyage. To quantify the standard deviation and mean value of the fuel savings,

Table 7

Dimensions of the applied dagger- and centerboards.

	RoRo	Tanker
Number of appendages	2	1
Span [m]	3.5	12
Chord [m]	0.6	2
AR	6	6
Long. position [% $L_{pp}$ ]	30	25
Transv. position [% B]	40/-40	0

Monte Carlo simulations with statistical distributions of the wind direction and speed along the routes must be performed. Such a study is presented in (Tillig et al., 2019), but it requires higher computational efforts since many points must be evaluated. Another possibility to reduce the uncertainty from the weather conditions is to use the method presented in Section 4.1 but with measurement intervals longer than one year. This will result in a more certain prediction of the long-term fuel savings but will not provide the standard deviations as the method presented in (Tillig et al., 2019) does.

It can be concluded that the largest uncertainties in the performance prediction using ShipCLEAN relate to the prediction of the lift and drag forces of a ship at a drift angle. The source of the largest uncertainty for the prediction of the expected fuel savings is the weather conditions the ship will experience.

## 5. Conclusions

The paper presented a continued development of a ship performance model called ShipCLEAN, which is a ship energy system model that can be used to predict the performance of generic cargo ships. The emphasis of the development presented in this study was on the detailed description of the modeling of wind-assisted propulsion accounting for various interaction effects, such as between the sails and the superstructure, and other hydrodynamic effects. The major conclusions of the study are that it is possible to predict with acceptable accuracy the performance of wind-assisted cargo ships with very limited input information and in short computational time, and large fuel savings can be achieved using Flettner rotors on ships.

The theory of the new models implemented in ShipCLEAN that describe wind-assisted propulsion were presented in detail, together with other hydrodynamic effects that need to be included for sailing ships. The Flettner rotor sail was used as the main wind-assisted technology of interest in several cases for two ship types—a tanker and a RoRo.

The interaction between Flettner rotors was modeled using potential flow theory. The results showed that the total thrust was only slightly affected by the presence of other rotors. However, since some rotors gained and others suffered in performance, the location of the center of effort was highly influenced by the interaction. Thus, it was concluded that interaction effects between sails must be considered for wind-assisted ships.

The sail module in ShipCLEAN was verified against model and full-scale measurements as well as CFD results. It was shown that, for a single Flettner rotor, the lift and drag coefficients in the full-scale measurements were considerably higher than those obtained by CFD computations or in model tests. Further, it was shown that the method to predict the aerodynamic interaction effects shows good agreement with the trends of the thrust and side force coefficients measured in model tests for two Flettner rotors.

The scope of the interaction effects related to the number of sails, their positions, ship type, etc. were difficult to generalize. It is therefore recommended to engage in several specific scenario-based analyses to understand how large interaction effects need to be to find a recommended or optimum condition/setup for the ship type and route of interest. Thus, many Flettner rotor configurations and simulations were carried out, which showed that the arrangement of the rotors on the ship influences the overall performance, an effect that is only possible to capture if interaction effects are respected. This finding highlighted the need for an additional model that enabled rpm control for the rotors due to interaction effects. The results with this additional model showed large gains in performance if each rotor's rpm was optimized for the local wind speed, the local wind angle, the ships drift angle and the rudder angle. Additional savings of approximately 2.5% were achieved with the rpm control compared to if the rotors are operated at the optimum SR for the local wind speed and angle. These findings show the complexity in the energy system of a ship and motivate using an energy-

systems-based ship performance analysis model that accounts for interaction effects between sails.

A comparison of results from several model tests and empirical methods showed large discrepancies in the predicted lift and drag force of a hull sailing at a drift angle. In this study, low aspect ratio wing theory is applied to ship hulls. A comparison was made between simulation results and model tests, which led to the conclusion that wing theory is able to model the lift and drag more accurately than the empirical method but that the hull form of a ship has a large impact on the actual lift and drag of a ship. It is concluded from an uncertainty study, that an accurate prediction of the lift to drag relation of a ship hull sailing at a drift angle is more important than the accurate prediction of the drift angle.

Simulations with realistic weather conditions and two example ships showed the versatility and applicability of the developed methods. The results showed potential savings of up to 30% for a tanker with 6 Flettner rotors on a Pacific Ocean route. For a RoRo on the Baltic Sea, the potential savings are shown to be approximately 14% with 4 Flettner rotors. From the study, it was concluded that the arrangement and position of the rotors have a large impact on the ship's performance and fuel savings. Comparing results from the tanker and the RoRo, it was concluded that the optimal arrangement differs largely depending on the ship design, speed and weather conditions along the route.

## Declaration of competing interest

The authors declare that they have no known competing financial interests or personal relationships that could have appeared to influence the work reported in this paper.

## CRediT authorship contribution statement

**Fabian Tillig:** Conceptualization, Methodology, Software, Validation, Resources, Writing - original draft, Visualization, Project administration. **Jonas W. Ringsberg:** Conceptualization, Resources, Writing - review & editing, Supervision, Project administration.

## Acknowledgements

This work was supported by The Swedish Energy Agency (grant number P44454-1) for funding the project "ShipCLEAN - Energy efficient marine transport through optimization of coupled transportation logistics and energy systems analyses". The authors thank the partners in the ShipCLEAN project for providing model test results and weather measurements. The authors also thank Viking Line for the opportunity to use full-scale measurements for verification of the sail force model.

## References

- Abbot, I.H., Von Doenhoff, A.E., 1959. *Theory of Wing Sections*. Dover Publications, Mineola, N.Y.
- Anderson, K., Bows, A., 2011. Beyond 'dangerous' climate change: emission scenarios for a new world. *Philos Trans Roy Soc: Math Phys Eng Sci* 1934 (369), 20–44. <https://doi.org/10.1098/rsta.2010.0290>.
- Ballnii, F., Olcer, A.I., Brandt, J., Neumann, D., 2017. Health costs and economic impact of wind assisted ship propulsion. *Ocean Eng.* 146, 477–485. <https://doi.org/10.1016/j.oceaneng.2017.09.014>.
- Barros, E., Pascoal, A., de Sa, E., 2008. Investigation of a method for predicting AUV derivatives. *Ocean Eng.* <https://doi.org/10.1016/j.oceaneng.2008.08.008>.
- Bentin, M., Zastrau, D., Schlaak, M., Reye, D., Elsner, R., Kotzur, S., 2016. A new routing optimization tool - influence of wind and waves in fuel consumption with and without wind assisted ship propulsion systems. *Transport. Res. Procedia* 14, 153–162. <https://doi.org/10.1016/j.trpro.2016.05.051>.
- Bertram, V., 2000. *Practical Ship Hydrodynamics*. Butterworth-Heimann, Oxford.
- Bethwaite, F., 2013. *High Performance Sailing: Faster Racing Techniques*. Bloomsbury, London.
- Bordogna, G., Muggiasca, S., Giappino, S., Belloli, M., Keuning, J., Huijsmans, R., 2019. Experiments on a Flettner rotor at critical and supercritical Reynolds numbers. *J. Wind Eng. Ind. Aerod.* 188, 19–29. <https://doi.org/10.1016/j.jweia.2019.02.006>.

- G. Bordogna, S. Muggiasca, S. Giappino, M. Belloli, J.A. Keuning, R.H.M. Huijsmans, The effects of the aerodynamic interaction on the performance of two Flettner rotors, *J. Wind Eng. Ind. Aerod.*, 196, 2020, DOI: 10.1016/j.jweia.2019.104024.
- Coastal Engineering Research Center, 1984. Shore Protection Manual. U.S. Army Corps of Engineers, Waterways Experiment Station, Vicksburg Mississippi.
- Garzon, F., Figueroa, A., 2017. The study on the flow generated by an array of four flettner rotors: theory and experiment. *Appl. Math.* 8, 1851–1858. <https://doi.org/10.4236/am.2017.812132>.
- Hoerner, S., 1985. Fluid-dynamic Lift. Hoerner Fluid Dynamics, New York City.
- Hoof, J., 1996. The cross-flow drag on a manoeuvring ship. *Ocean Eng.* 21 (3), 329–342. [https://doi.org/10.1016/0029-8018\(94\)90004-3](https://doi.org/10.1016/0029-8018(94)90004-3).
- Houghton, E.L., Carpenter, P.W., Collicott, S.H., Valentine, D.T., 2017. Aerodynamics for Engineering Students, seventh ed. Butterworth-Heinemann, ISBN 9780081001943, pp. 449–523. <https://doi.org/10.1016/B978-0-08-100194-3.00007-9> (Chapter 7) - Wing Theory.
- Inoue, S., Hirano, M., 1987. A practical calculation method of ship manoeuvring motion. *Int. Shipbuild. Prog.* 28 (325) <https://doi.org/10.3233/ISP-1981-2832502>.
- Jorgensen, L.H., 1973. Prediction of Static Aerodynamic Characteristics for Space-shuttle-like and Other Bodies at Angle of Attack from 0 to 180 Degrees. NASA, Washington D.C.
- Kaltschmitt, M., Streicher, W., Wiese, A., 2007. Red., Renewable Energy: Technology, Economics and Environment. Springer, Berlin, Heidelberg.
- Kijima, K., Nakiri, Y., Katsumo, T., Furukawa, Y., 1990. On the manoeuvring performance of a ship with the parameter of loading condition. *J. Soc. Nav. Archit. Jpn.* 168, 141–148.
- Kramer, J., Steen, S., Savio, L., 2016. Drift forces - wingsails vs flettner rotors. In: International Conference on High Performance Marine Vehicles, 17-19 October, Cortona, Italy.
- Kume, K., Hasegawa, J., Tsukada, Y., Fujisawa, J., Fukasawa, R., 2006. Measurements of hydrodynamic forces, surface pressure, and wake for obliquely towed tanker model and uncertainty analysis for CFD validation. *J. Mar. Sci. Technol.* 11, 65–75. <https://doi.org/10.1007/s00773-005-0209-y>.
- Lee, H., Jo, Y., Lee, D.-J., Choi, S., 2016. Surrogate model based design optimization of multiple wing sails considering flow interaction effects. *Ocean Eng.* 121, 422–436. <https://doi.org/10.1016/j.oceaneng.2016.05.051>.
- Lewandowski, E.M., 2004. The Dynamics of Marine Craft: Maneuvering and Seakeeping. World Scientific Publishing, Singapore.
- Li, D., Leer-Andersen, M., Allenström, B., 2012. Performance and vortex formation of Flettner rotors at high Reynolds numbers. In: 29th International Symposium on Naval Hydrodynamics, Gothenburg, 26-31 August.
- Longo, J., Stern, F., 2002. Effects of drift angle on model ship flow. *Exp. Fluid* 32, 558–569. <https://doi.org/10.1007/s00348-001-0397-0>.
- Lu, R., Ringsberg, J.W., 2019. Ship energy performance study of three wind-assisted ship propulsion technologies including a parametric study of the Flettner rotor technology. *Ships Offshore Struct.* <https://doi.org/10.1080/17445302.2019.1612544>.
- Mathworks, 2020. Matlab documentations [Online]. <https://www.mathworks.com/help/matlab/>. (Accessed 18 March 2020).
- Meroney, R., 1985. Wind flow patterns about buildings. *J. Wind Eng. Ind. Aerod.* 21, 21–38. [https://doi.org/10.1016/0167-6105\(85\)90031-5](https://doi.org/10.1016/0167-6105(85)90031-5).
- Norsepower, 2019a. Viking Grace Rotor Sail Performance Analysis Results. Norsepower, Helsinki, Finland. [https://7c859085-dddb-4d30-8667-a689091113a8.filesusr.com/ugd/cea95e\\_a721091625ee452db73c9fb69804268e.pdf](https://7c859085-dddb-4d30-8667-a689091113a8.filesusr.com/ugd/cea95e_a721091625ee452db73c9fb69804268e.pdf). (Accessed 2 January 2020).
- Norsepower, 2019b. Norsepower Rotor Sail Technology. Norsepower, Helsinki. [https://7c859085-dddb-4d30-8667-a689091113a8.filesusr.com/ugd/cea95e\\_90015201cbe64b83b56cfe01fe0e995.pdf](https://7c859085-dddb-4d30-8667-a689091113a8.filesusr.com/ugd/cea95e_90015201cbe64b83b56cfe01fe0e995.pdf). (Accessed 2 January 2020).
- IMO, 2018 [Online]. <http://www.imo.org/en/OurWork/Environment/PollutionPrevention/AirPollution/Pages/GHG-Emissions.aspx>. (Accessed 2 January 2020).
- Rehmatulla, N., Parker, S., Smith, T., Stulgis, V., 2017. Wind technologies: opportunities and barriers to a low carbon shipping industry. *Mar. Pol.* 75, 217–226. <https://doi.org/10.1016/j.marpol.2015.12.021>.
- Searcy, T., 2017. Harnessing the wind: a case study of applying Flettner rotor technology to achieve fuel and cost savings for Fiji's domestic shipping industry. *Mar. Pol.* 86, 164–172. <https://doi.org/10.1016/j.marpol.2017.09.020>.
- Swanson, W.M., 1961. The magnus effect: a summary of investigations to date. *J. Basic Eng.* 83 (3), 461–470.
- Talluri, L., Nalianda, D., Giuliani, E., 2018. Techno economic and environmental assessment of Flettner rotors for marine propulsion. *Ocean Eng.* 154, 1–15. <https://doi.org/10.1016/j.oceaneng.2018.02.020>.
- Tillig, F., 2017 [Licentiate thesis]. A Generic Model for Simulation of the Energy Performance of Ships- from Early Design to Operational Conditions, 2. Chalmers University, Gothenburg, Sweden. Report No. 2017.
- Tillig, F., Ringsberg, J.W., 2018. A 4 DOF Simulation Model Developed for Fuel Consumption Prediction of Ships at Sea. *Ships and Offshore Structures*. <https://doi.org/10.1080/17445302.2018.1559912>.
- Tillig, F., Ringsberg, J.W., Mao, W., Ramne, B., 2017. A generic energy systems model for efficient ship design and operation. *J. Environ. Maritime. Environ.* 231 (2), 649–666. <https://doi.org/10.1177/1475090216680672>.
- Tillig, F., Ringsberg, J.W., Mao, W., Ramne, B., 2018. Analysis of uncertainties in the prediction of ship's fuel consumption - from early design to operation conditions. *Ships Offshore Struct.* 13 (no Suppl. 1), 13–24. <https://doi.org/10.1080/17445302.2018.1425519>.
- Tillig, F., Ringsberg, J.W., Psarafitis, H.N., Zis, T., 2019. ShipCLEAN - an integrated model for transport efficiency, economics and CO2 emissions in shipping. In: Proceedings of Moses2019 Conference, Glasgow, 8-10 May.
- Traut, M., Gilbert, P., Walsh, C., Bows, A., Filippone, A., Stansby, P., Wood, R., 2014. Propulsive power contribution of a kite and a Flettner rotor on selected shipping routes. *Appl. Energy* 113, 362–372. <https://doi.org/10.1016/j.apenergy.2013.07.026>.
- van der Kolk, N., 2016. Hydrodynamics of wind-assisted ship propulsion: modeling of Hydrodynamic sideforce. In: 24th International HISWA Symposium on Yacht Design and Yacht Construction, 14-15 Nov, Amsterdam.
- van der Kolk, N., Bordogna, G., Mason, J., Desprairies, P., Vrijdag, A., 2019a. Case study: wind-assisted ship propulsion performance prediction, routing, and economic modelling. In: Power&Propulsion Alternatives for Ships, London, 22.- 23. January.
- van der Kolk, N., Keuning, J., Huijsmans, R., 2019b. Part 1: experimental validation of a RANS-CFD methodology for the hydrodynamics of wind-assisted ships operating at leeway angles. *Ocean Eng.* 178, 375–387. <https://doi.org/10.1016/j.oceaneng.2018.12.041>.
- Viola, I.M., Sacher, M., Xu, J., Wang, F., 2015. A numerical method for the design of ships with wind-assisted propulsion. *Ocean Eng.* 105, 33–42. <https://doi.org/10.1016/j.oceaneng.2015.06.009>.